

# Chapter 14

## A Hydromechanical Model for Lower Crustal Fluid Flow

J.A.D. Connolly and Y.Y. Podladchokov

Correct  
Podladchokov to  
Podladchikov, here  
and in running  
header

**Abstract** Metamorphic devolatilization generates fluids at, or near, lithostatic pressure. These fluids are ultimately expelled by compaction. It is doubtful that fluid generation and compaction operate on the same time scale at low metamorphic grade, even in rocks that are deforming by ductile mechanisms in response to tectonic stress. However, thermally-activated viscous compaction may dominate fluid flow patterns at moderate to high metamorphic grades. Compaction-driven fluid flow organizes into self-propagating domains of fluid-filled porosity that correspond to steady-state wave solutions of the governing equations. The effective rheology for compaction processes in heterogeneous rocks is dictated by the weakest lithology. Geological compaction literature invariably assumes linear viscous mechanisms; but lower crustal rocks may well be characterized by non-linear (power-law) viscous mechanisms. The steady-state solutions and scales derived here are general with respect to the dependence of the viscous rheology on effective pressure. These solutions are exploited to predict the geometry and properties of the waves as a function of rock rheology and the rate of metamorphic fluid production. In the viscous limit, wavelength is controlled by a hydrodynamic length scale  $\delta$ , which varies inversely with temperature, and/or the rheological length scale for thermal activation of viscous deformation  $l_A$ , which is on the order of a kilometer. At high temperature, such that  $\delta < l_A$ , waves are spherical. With falling temperature, as  $\delta \rightarrow l_A$ , waves flatten to sill-like structures. If the fluid overpressures associated with viscous wave propagation reach the conditions for plastic failure, then compaction induces channelized fluid flow. The channeling is caused by vertically elongated porosity waves that nucleate with characteristic spacing  $\delta$ . Because  $\delta$  increases with falling temperature, this mechanism is amplified towards the surface. Porosity wave passage is associated with pressure

---

J.A.D. Connolly (✉)

Department of Earth Sciences, Swiss Federal Institute of Technology, Zurich 8092, Switzerland

Y.Y. Podladchokov

Geophysics Institute, University of Lausanne, Lausanne 6617, Switzerland

30 anomalies that generate an oscillatory lateral component to the fluid flux that is  
31 comparable to the vertical component. As the vertical component may be orders of  
32 magnitude greater than time-averaged metamorphic fluxes, porosity waves are a  
33 potentially important agent for metasomatism. The time and spatial scales of these  
34 mechanisms depend on the initial state that is perturbed by the metamorphic  
35 process. Average fluxes place an upper limit on the spatial scale and a lower limit  
36 on the time scale, but the scales are otherwise unbounded. Thus, inversion of natural  
37 fluid flow patterns offers the greatest hope for constraining the compaction scales.  
38 Porosity waves are a self-localizing mechanism for deformation and fluid flow. In  
39 nature these mechanisms are superimposed on patterns induced by far-field stress  
40 and pre-existing heterogeneities.

## 41 **14.1 Introduction**

42 The volume change associated with isobaric metamorphic devolatilization is usu-  
43 ally positive, consequently devolatilization has a tendency to generate high pressure  
44 pore fluids. This generality has led to the notion that high fluid pressures are the  
45 ultimate cause of metamorphic fluid flow. A simple experiment with a well-shaken  
46 bottle of soda pop (i.e., a sweet, carbonated, beverage) demonstrates that this notion  
47 is ill conceived. Once the bottle is opened some pop is lost, but, after a short time,  
48 flow ceases leaving most of the initial pop in the bottle. In the metamorphic  
49 analogy, the bottle is the porous rock matrix and the pop is its pore fluid. How  
50 then is this pore fluid expelled? As early as 1911, Goldschmidt (1954) realized that  
51 fluid expulsion could only occur if the rock compacts and squeezes the pore fluid  
52 out. The compaction process is a form of deformation that, usually, is driven by the  
53 weight of the overlying rock. In this case, the downward flow of the rock matrix, in  
54 response to gravity, is responsible for the upward flow of the less dense pore fluid.  
55 **Compaction driven fluid flow** is complex because it is inseparable from rock  
56 deformation and because the hydraulic properties that limit fluid flow through the  
57 rock matrix, such as permeability and porosity, are dynamic. This chapter outlines a  
58 physical model for the compaction process in the Earth's lower crust. While the  
59 specifics of this chapter are of direct relevance only to continental crust, the  
60 concepts apply to oceanic crust as well.

61 Metamorphic devolatilization usually results in a significant decrease in the  
62 volume of the residual solid, e.g., serpentine dehydration causes a reduction in  
63 the solid volume in excess of 10%. Without compaction, this change in volume  
64 would be preserved as grain-scale porosity. Thus, the near absence of grain-scale  
65 porosity in exhumed metamorphic rocks (Norton and Knapp 1977) is unequivocal  
66 evidence for irreversible compaction. Despite this evidence, irreversible compac-  
67 tion is almost universally disregarded in quantitative models of metamorphic fluid  
68 flow. This neglect is reasonable provided the fluid flow of interest occurs on a short  
69 time scale compared to the time scale for compaction. Because viscous compaction  
70 is thermally-activated, neglecting compaction becomes more problematic, but not

necessarily invalid, with increasing metamorphic grade. Likewise, although compaction is an appealing explanation for ubiquitous evidence of high fluid pressure during metamorphism (e.g., Etheridge et al. 1984; Sibson 1992; McCuaig and Kerrich 1998; Simpson 1998; Cox 2005; Rubinstein et al. 2007; Peng et al. 2008; Scarpa et al. 2008; Padron-Navarta et al. 2010), high fluid pressures cannot be explained unless metamorphic systems are poorly drained. However, if metamorphic systems are poorly drained, high fluid pressures may simply be a consequence of ephemeral fluid production. This argument is not brought forward to justify the neglect of compaction in modeling metamorphic fluid flow, but rather to emphasize that the conditions at which compaction becomes important are uncertain. An intriguing set of observations (Young and Rumble 1993; van Haren et al. 1996; Graham et al. 1998) indicate that localized fluid-rock interaction at amphibolite-facies conditions occurred on a time scale of  $10^3$ – $10^5$  year during much longer ( $\sim 10^7$  year) regional metamorphic events. An explanation for the limited duration of fluid-rock interaction is that compaction sealed the rocks on the  $10^3$ – $10^5$  year time scale. Transiently high metamorphic permeability on similar time scales (Ingebritsen and Manning 2010) and geophysically observable sub-Himalayan densification on a time scale of  $< 1$  My at eclogite facies conditions (Hetenyi et al. 2007) provide additional evidence that compaction is an efficient process at moderate metamorphic temperatures. Compaction is synonymous with fluid expulsion, thus if metamorphic fluid flow is compaction dominated, exotic fluid sources and crustal scale fluid recirculation should have limited impact on the metamorphic fluid budget (Walther and Orville 1982). That metamorphic fluid fluxes, inferred from field studies (e.g., Ferry 1994; Skelton 1996; Wing and Ferry 2007; Manning and Ingebritsen 1999), are comparable to the vertically integrated metamorphic fluid production (Walther and Orville 1982; Yardley 1983; Connolly and Thompson 1989) is suggestive that metamorphic flow regimes are indeed compaction dominated.

The assumption of classical metamorphic petrology, that fluid pressure is equal to the total pressure, implies that rocks compact in response to negligible effective pressure, i.e., that rocks have no strength. In this limit, compaction driven flow of a low-density fluid can only be upward (Walther and Orville 1982). A surprising feature of compaction-driven fluid flow in rocks of finite strength is that a perturbation, e.g., a metamorphic devolatilization reaction, to a uniform flow regime induces a regime in which fluid flow occurs by the propagation of domains of fluid-filled porosity (Richter and McKenzie 1984; Scott and Stevenson 1986; Suetnova et al. 1994; Wiggins and Spiegelman 1995; Connolly 1997). The properties of these domains closely approximate steady-state wave solutions to the equations that describe fluid flow in compacting media (Barcilon and Richter 1986; Barcilon and Lovera 1989). In this porosity wave propagated flow regime, while the overall tendency is to drive fluid upward or, in the presence of tectonic stress, toward low mean stress (Connolly and Podladchikov 2004), lateral fluid flow occurs on the time and spatial scales of the steady-state waves. In a homogeneous crust that is not subject to tectonic forcing, such waves would be the primary mechanism of metamorphic fluid flow. This idealization is far from reality, but

116 the steady-state wave solutions define background patterns upon which the effects  
117 of lithological heterogeneity and tectonic deformation are imposed. Consequently,  
118 the spatial and temporal scales of the compaction process limit the extent to which  
119 perturbations may influence the idealized compaction-driven flow regime. For  
120 example, a transient shear zone may induce both lateral and downward fluid flow  
121 (Austrheim 1987; Sibson 1992), but it can only do so on time and spatial scales  
122 shorter than those for compaction (Connolly 2010). Understanding the time and  
123 length scales of steady-state wave solutions to the compaction equations is thus  
124 essential to understanding lower crustal fluid flow, even if the flow is not dominated  
125 by compaction.

126 The physical explanation for the existence of porosity waves requires only an  
127 elementary understanding of the driving forces and constitutive relations that  
128 govern fluid flow, but the derivation of the steady-state solutions involves cumbersome  
129 math (Barcilon and Richter 1986; Barcilon and Lovera 1989). The intent here  
130 is to avoid this math, which is summarized in the Appendix, and to focus on the  
131 physical constraints that influence the steady-state solutions. The first part of this  
132 Chapter reviews the rheological and hydraulic concepts relevant to the compaction  
133 process. Large scale modeling of metamorphic fluid flow inevitably invokes a  
134 steady-state hydraulic regime to define the pre-metamorphic state. This initial  
135 steady state is critical to model outcomes because it determines the response of  
136 the system to the metamorphic perturbation. Unfortunately, because metamorphism  
137 is the most probable source of lower crustal fluids, the assumption of an initial  
138 steady state leaves much to be desired. In truth, in the modeling of metamorphic  
139 fluid flow, less is known about the initial state than is known about the metamorphic  
140 state. The second part of this Chapter draws attention to the uncertainties inherent in  
141 defining the pre-metamorphic lower crustal hydraulic regime, and the final part  
142 details the expected scales and patterns of compaction-driven flow as function of  
143 initial conditions and rheology.

## 144 **14.2 Compaction Pressures and Rheologic and Hydraulic** 145 **Constitutive Relations**

146 In compaction problems, **fluid** is distinguished from the solid phase(s) by its shear  
147 strength; specifically the fluid is defined as a phase that cannot support deviatoric  
148 stress. This definition has the implication that on the time scale relevant for  
149 compaction, fluid pressure is uniform throughout the connected porosity at the  
150 scale of the solid grains and is independent of the solid pressure. The term **porosity**  
151 is used here to mean only this connected porosity; rocks may contain porosity that is  
152 not interconnected, but because this porosity does not influence fluid flow it is of  
153 little interest. Further, it is assumed that the porosity is always filled by fluid, i.e.,  
154 porosity is simply the volume fraction of fluid in the solid matrix. Although the  
155 word porosity conjures up an image of grain-scale structures, it may apply to

paragraph. Paragraph breaks have been added throughout after any equation followed by a full stop. These paragraph should be deleted.

substantially larger features, such as fractures, provided these features are small in comparison to the length scale for fluid flow. 156 157

**Compaction** is formally the change in porosity caused by **dilational** (volume changing) **strain** of a solid matrix, i.e., the isotropic component of the strain tensor. It follows from the Curie principle that compaction can only be a direct function of invariant characteristics of the stress state. From Terzaghi's effective stress concept, the simplest invariant is the effective pressure, i.e., the difference between total pressure and fluid pressure, which is assumed here to be the sole cause of compaction. The total pressure can be decomposed into components due to the fluid and solid as 158 159 160 161 162 163 164 165

$$p = (1 - \phi)p_s + \phi p_f \quad (14.1)$$

where  $\phi$  is porosity and subscripts s and f denote solid and fluid, respectively (see Table 14.1 for notation). Making use of Eq. 14.1, and observing that **mean stress**,  $\bar{\sigma}$ , and **pressure** are formally equivalent, **effective pressure** is 166 167 168

$$p_e \equiv \bar{\sigma} - p_f = (1 - \phi)(p_s - p_f). \quad (14.2)$$

Because high fluid pressures may lead to negative effective pressures, it is sometimes convenient to describe compaction processes in terms of **fluid overpressure**, which is defined here as  $-p_e$ . 169 170 171

**Darcy's law** (e.g., McKenzie 1984) relates the volumetric **fluid flux** relative 172

$$\mathbf{q} = -(1 - \phi) \frac{k}{\mu} (\nabla p_f - \rho_f \mathbf{g} \mathbf{u}_z)$$

cinch up? this is minus p subscript e

through a porous matrix to the difference between the actual fluid pressure gradient and the hydrostatic pressure gradient of the fluid ( $\rho_f \mathbf{g} \mathbf{u}_z$ ), where  $k$  is the hydraulic permeability of the solid matrix,  $\rho_f$  and  $\mu$  are the density and shear viscosity of the fluid, and  $\mathbf{u}_z$  is a downward directed unit vector. It is often useful to characterize the dynamics of fluid flow by the macroscopic velocity,  $\mathbf{v}$ , of the fluid rather than flux. As the fluid flux is the product of the fluid velocity and porosity, any expression in terms of flux can be converted to one in terms of velocity via 173 174 175 176 177 178 179

$$\mathbf{v} = \mathbf{q}/\phi \quad (14.4)$$

**Flux** **no new paragraph** is typically negative (upward) for a downward directed depth coordinate. This is a potential source of confusion in that a large upward flux is, numerically, less than a small flux. To minimize such confusion, the magnitude of a vectorial quantity, indicated by italics (e.g.,  $q$  for flux  $\mathbf{q}$  and  $v$  for velocity  $\mathbf{v}$ ), is used when direction is evident. Darcy's law relates flux to pressure gradients rather than pressure. This has the implication that a high-pressure fluid need not flow provided its pressure gradient is hydrostatic. 180 181 182 183 184 185 186

t1.1 **Table 14.1** Frequently used symbols

t1.2	Symbol	Meaning
t1.3	$A$	Coefficient of viscous flow, Eqs. 14.11 and 14.12
t1.4	$c_\phi$	Geometric and grain-size dependent factor in the permeability function, Eq. 14.17
t1.5	$c_\sigma$	Geometric factor in the compaction rate function, Eq. 14.16
t1.6	$D$	Pre-exponential term in Arrhenius dependence of $A$ , Eqs. 14.12 and 14.14
t1.7	$e$	Base of natural logarithms (2.718...)
t1.8	$g$	Magnitude of gravitational acceleration
t1.9	$k; k_0$	Permeability, Eq. 14.17; background value
t1.10	$l_A$	Viscous e-fold length, Eq. 14.15
t1.11	$n_\phi$	Porosity exponent in the permeability function, Eq. 14.17
t1.12	$n_\sigma$	Stress exponent in the viscous flow law, Eq. 14.11
t1.13	$O(n)$	Literally, "of the order of magnitude of $n$ "
t1.14	$p; p_e; p_f; p_s$	Total pressure, Eq. 14.1; effective pressure, $p - p_f$ , Eq. 14.2; fluid pressure; solid pressure
t1.14	$\mathbf{q}; q; q_0; \bar{q}$	Fluid flux, Eqs. 14.3, 14.5, 14.8, and 14.37; fluid flux magnitude; background value; time-averaged value
t1.15		
t1.16	$q_e$	Time-averaged fluid flux (magnitude) associated with a 1-d wave, Eq. 14.25
t1.17	$Q$	Activation energy for viscous deformation of the solid matrix
t1.18	$R$	Universal gas constant
t1.19	$R$	Viscosity contrast
t1.20	$T$	Temperature, K
t1.21	$\mathbf{u}_z$	A downward directed unit vector
t1.22	$V_e; V_e^{1d}$	Fluid volume associated with a wave, Eq. 14.27; 1-d volume, Eq. 14.26
t1.23	$v; v_0; v_\phi$	Fluid speed; background value; wave speed, Eq. 14.56
t1.24	$z$	Depth coordinate, positive downward
t1.25	$\dot{\epsilon}$	Shear strain rate, Eq. 14.11
t1.26	$\dot{\epsilon}_\phi$	Compaction rate, Eq. 14.16
t1.27	$\delta; \delta_d$	Viscous compaction length, Eq. 14.23; decompaction length for decompaction-weakening, Eq. 14.30
t1.28	$\Delta\rho; \Delta\sigma$	$\rho_s - \rho_f$ ; differential stress
t1.29	$\eta$	Solid shear viscosity
t1.30	$\lambda$	Wavelength
t1.31	$\mu$	Fluid shear viscosity
t1.32	$\phi; \phi_0$	Porosity (hydraulically connected); background value
t1.33	$\rho_s; \rho_f$	Solid density; fluid density
t1.34	$\bar{\sigma}; \sigma_y$	Mean stress ( $p$ ), Eq. 14.38; tensile yield stress
t1.35	$\tau$	Compaction time scale, $\delta/v_0$ , Eq. 14.24
t1.36	$\nabla; \nabla \cdot$	Gradient ( $\partial/\partial z$ in 1-d); divergence ( $\partial/\partial z$ in 1-d)

187 In compaction problems, it is useful to reformulate Darcy's law in terms of the  
 188 effective pressure responsible for compaction as

no new paragraph

$$\mathbf{q} = -(1 - \phi) \frac{k}{\mu} (\nabla \bar{\sigma} - \nabla p_e - \rho_f g \mathbf{u}_z). \quad (14.5)$$

189 For the classical  $p = p_f$  metamorphic model (i.e.,  $\nabla p_e = 0$ ), this form  
 190 demonstrates that the direction of fluid flow is a function of the mean stress

gradient, which may be influenced by tectonic processes. These effects complicate 191  
 discussion because they depend on the specifics of the tectonically-induced stress 192  
 field. To eliminate this complication, it is assumed that the mean stress gradient is 193  
 due entirely to the vertical load, i.e., that pressure is lithostatic. Tectonic stress 194  
 affects the direction of compaction driven flow, but does not affect the compaction 195  
 mechanism, thus the lithostatic assumption is not essential to any of the phenomena 196  
 discussed here. Making the additional assumptions that solid density is not strongly 197  
 variable and that porosity is small (i.e.,  $1 - \phi \approx 1$ ), total and effective pressures are 198

$$p \approx p_s \approx \rho_s g z \quad (14.6)$$

$$p_e \approx \rho_s g z - p_f, \quad (14.7)$$

where  $\rho_s$  is the density of the solid matrix and  $z$  is depth. Rearranging Eq. 14.7 to 199  
 give fluid pressure in terms of effective pressure, Darcy's law then simplifies to 200

$$\mathbf{q} = \frac{k}{\mu} (\nabla p_e - \Delta \rho \mathbf{g}_z). \quad (14.8)$$

At near surface conditions, fluid pressures are near hydrostatic, i.e., 201  
 $\nabla p_e \approx \Delta \rho \mathbf{g}_z$ , and small perturbations in pressure can cause fluids to flow in any 202  
 direction. This regime is often referred to as one of normal fluid pressure, whereas 203  
 at conditions of lithostatic fluid pressure, in which case  $\nabla p_e = 0$ , 204

$$q = k \Delta \rho g / \mu \quad (14.9)$$

and flux is vertical and essentially controlled by permeability. 205

Equations 14.3 and 14.4, give the fluid velocity and flux relative to the reference 206  
 frame of the solid, but in geological compaction problems solid velocities are finite 207  
 relative to the Earth's surface. It is assumed here that the solid velocity is negligible. 208  
 This assumption is justified in the small porosity limit (Connolly and Podladchikov 209  
 2007). The Appendix provides a more rigorous treatment that does not neglect solid 210  
 velocity. 211

### 14.2.1 Rheology 212

Just as in the case of non-dilational rheology, the endmember **compaction** 213  
**rheologies** are elastic, plastic, and viscous. Strictly elastic, plastic, and viscous 214  
 describe, respectively, reversible time-independent, irreversible time-independent, 215  
 and irreversible time-dependent deformation (Hill 1950). In the geological litera- 216  
 ture these terms, particularly plastic, are often confused with terms such as **ductile** 217  
 and **brittle** that describe deformation style. In geological materials, the origin of 218  
 ductile behavior is most commonly viscous rheology, but may also be a plastic 219

220 mechanism, while brittle deformation is a manifestation of plasticity and is usually  
 221 localized (Ranalli 1995).

222 **Elastic compaction** and fluid expulsion results from both solid ( $\beta_s$ ) and fluid ( $\beta_f$ )  
 223 compressibilities and a peculiar component referred to as pore compressibility that  
 224 is a property of the fluid–rock aggregate (Gueguen et al. 2004). Although pore  
 225 compressibility dominates the compaction of poorly consolidated sediments, in  
 226 rocks with porosities below a few percent, pore compressibilities become compa-  
 227 rable to the solid compressibility, which is  $O(10^{-11}) \text{ Pa}^{-1}$  (Wong et al. 2004; the  
 228 notation  $O(n)$ , which means, literally, “of the order of magnitude of  $n$ ”, is used  
 229 extensively in this chapter because of our concern with scales based on highly  
 230 uncertain parameters). Thus, for lower crustal rocks, the elastic compaction caused  
 231 by a change in effective pressure  $\Delta p_e$  is

no new paragraph

$$\Delta\phi/\phi \approx -\beta_s\Delta p_e. \quad (14.10)$$

232 From Eq. 14.10, a reduction in  $p_f$  from lithostatic to hydrostatic conditions at  
 233 20 km depth ( $\Delta p_e = \Delta\rho gz$ ) decreases by 0.4% of its initial value. As fluid  
 234 compressibilities are roughly an order of magnitude greater than solid compress-  
 235 ibility at the conditions of the lower crust (Walther and Orville 1982), the net fluid  
 236 expulsion necessary to effect the pressure drop is only  $\sim 4.4\%$  of the fluid mass  
 237 initially present in the porosity. Thus, at typical lower crustal conditions, elastic  
 238 dilational strain can be neglected as a mechanism for lower crustal fluid expulsion.  
 239 In this regard it is important to distinguish fluid expulsion from fluid flow as,  
 240 particularly in the non-compacting limit, thermoelastic expansivity of the fluid  
 241 may create pressure gradients responsible for fluid circulation (e.g., Hanson 1997;  
 242 Staude et al. 2009; Nabelek 2009).

243 Excepting irreversible phase transformations, viscous and plastic bulk strains in  
 244 rocks are caused by microscopic shear deformation that eliminates porosity. Plastic  
 245 rheologies are complex, but fortunately only cataclastic and Mohr-Coulomb plastic  
 246 rheologies are of relevance here. **Cataclasis** (Wong et al. 2004), the crushing of  
 247 grains in response to increasing load, is a well-known phenomenon in sedimentary  
 248 basins where it gives rise to an exponential decay of porosity with depth (Athy  
 249 1930; Connolly and Podladchikov 2000). Crushing is inescapable once stress  
 250 concentrations approach the ultimate strength of the solid material (Hill 1950),  
 251 which is itself 10% of the shear modulus of the solid. Thus, the role of cataclastic  
 252 compaction must be acknowledged once stress concentrations are  $O(1)$  GPa. In  
 253 sedimentary rocks, the requisite stress concentrations are caused by irregular grain  
 254 contacts. These asperities are gradually eliminated during compaction, leading to  
 255 strain-hardening. In sediments, this strain-hardening typically limits cataclastic  
 256 compaction to rocks with porosities in excess of a few percent (Hunt 1990; Powley  
 257 1990). Cataclasis is thus unlikely in lower crustal metamorphic rocks unless  
 258 effective pressures are exceptional.

259 Although brittle failure is usually thought of as a mechanism for accommodating  
 260 shear strain, positive dilational strain (i.e., **dilatancy**) is an inescapable consequence  
 261 of non-associated plastic (brittle) failure. If an imposed differential stress is large in

comparison to the tensile strength of the rock matrix, brittle failure may limit fluid pressure to sublithostatic values (Sibson 2004, cf. Rozhko et al. 2007). Given that rock tensile strengths rarely exceed 50 MPa, and may be near zero, in some circumstances truly lithostatic fluid pressures may only be possible in the absence of significant differential stress, whereupon fluid pressure is limited by hydrofracturing, which occurs when the fluid overpressure exceeds tensile strength. **Viscous compaction** is unimportant at surface conditions, but, because it is a thermally activated mechanism, it becomes inevitable with increasing temperature. The viscous rheology of the crust is usually described by a power-law constitutive relationship of the form (e.g., Kohlstedt et al. 1995; Ranalli 1995)

$$\dot{\epsilon} = A|\Delta\sigma|^{n_\sigma-1}\Delta\sigma, \quad (14.11)$$

where  $\dot{\epsilon}$  is the strain rate in response to differential stress  $\Delta\sigma$ ,  $n_\sigma$  is the stress exponent, and  $A$  is the coefficient of viscous flow. The coefficient  $A$  is a temperature dependent material property that may also be sensitive to grain size (e.g., pressure solution creep) and chemical factors (e.g., the chemical potential of oxygen and/or water). These latter dependencies are uncertain and therefore disregarded in large-scale modeling, but the temperature dependence is usually retained and described by the Arrhenius relation

$$A = D \exp\left(\frac{-Q}{RT}\right), \quad (14.12)$$

where  $Q$  is the activation energy for the viscous mechanism, and  $D$  is a material property that is independent of temperature. To provide a simple model for the viscous rheology of the lower crust,  $D$  is parameterized here in terms of the strain-rate, stress, temperature, and depth of the brittle-ductile transition, i.e., the depth at which viscous mechanisms become capable of accommodating tectonic strain rates (Kohlstedt et al. 1995). In compressional settings, at this depth,  $z_{BD}$ , assuming  $\sigma_2 = (\sigma_1 + \sigma_3)/2$  and the hydrostatic fluid pressure, the **Mohr-Coulomb rheology** of the upper crust defines the differential stress as (Petrini and Podladchikov 2000)

$$\Delta\sigma_{BD} = gz_{BD} \frac{\rho_f(3 \sin \theta - 1) - 2\rho_{UC} \sin \theta}{\sin \theta - 1} \quad (14.13)$$

where, by Byerlee's law, the internal angle of friction  $\theta = \pi/6$  (Ranalli 1995) and  $\rho_{UC}$  is the density of upper crustal rock. For  $\rho_f/\rho_{UC} = 0.3$ , Eq. 14.13 simplifies to  $\Delta\sigma_{BD} = 1.7\rho_{UC}gz_{BD}$ . Substituting this estimate for  $\Delta\sigma$  in Eq. 14.11 and making use of Eq. 14.12

$$D = \frac{\dot{\epsilon}_{BD}}{(1.7z_{BD}\rho_{UC}g)^{n_\sigma}} \exp\left(\frac{Q}{RT_{BD}}\right). \quad (14.14)$$

291 The validity of this parameterization hinges on whether Eqs. 14.11 and 14.12  
 292 provide an adequate description of the ductile mechanism, but does not require or  
 293 imply that metamorphism occurs in a compressional tectonic setting or that the  
 294 brittle-ductile transition during metamorphism occurs at the conditions chosen for  
 295 the parameterization. Activation energies and stress exponents are relatively well  
 296 known from rock deformation experiments. Typical values for crustal rocks are in  
 297 the range  $n_\sigma = 2.5 - 4$  and  $Q = 150 - 400$  kJ/mol. The depth, temperature, and  
 298 strain rate at the base of the **seismogenic zone**, which is usually taken to correspond  
 299 with the brittle portion of the crust (Sibson 1986; Scholz 1988; Zoback and  
 300 Townend 2001), are  $z_{BD} \approx 3 - 20$  km,  $T_{BD} \approx 623 - 723$  K and  $\dot{\epsilon}_{BD} \approx 10^{-12}$  to  
 301  $10^{-16}$  s<sup>-1</sup>, but these ranges are not **entirely** independent due to autocorrelation  
 302 (Liotta and Ranalli 1999; Ranalli and Rybach 2005). The values  $n_\sigma = 3$ ,  $Q = 250$   
 303 kJ/mol,  $T_{BD} = 623$  K,  $\dot{\epsilon}_{BD} = 10^{-15}$  s<sup>-1</sup>,  $z_{BD} = 15$  km, and  $\rho_{UC} = 2,700$  kg/m<sup>3</sup> are  
 304 taken here to represent a plausible, but by no means unique, condition for the  
 305 brittle-ductile transition.

306 It is often useful to characterize the variation in viscous rheology due to the  
 307 increase in temperature with depth in terms of a depth interval rather than a  
 308 temperature change. For this purpose, differentiation of Eq. 14.12, with respect to  
 309 depth, yields the desired measure

$$l_A = A \left/ \frac{\partial A}{\partial z} \right. = \frac{RT^2}{Q \frac{\partial T}{\partial z}}, \quad (14.15)$$

310 which is the change in depth necessary to increase strain rates by a factor of  
 311  $e$  (2.718...). For the parameter choices specified above, the **viscous e-fold length**  
 312  $l_A$  is  $O(1)$  km at the conditions of lower crustal metamorphism (Fig. 14.1). In the  
 313 upper crust, pressure solution gives rise to a linear viscous ( $n_\sigma = 1$ ) rheology that is  
 314 characterized by activation energies in the range 20–40 kJ/mol (Rutter 1983; Spiers  
 315 and Schutjens 1990; Shimizu 1995; Connolly and Podladchikov 2000). From  
 316 Eq. 14.15, such small activation energies increase  $l_A$  by an order of magnitude,  
 317 implying a weak depth dependence that is inconsistent with the restricted depth  
 318 range and temperature dependence of the seismogenic zone (Sibson 1986; Scholz  
 319 1988; Ranalli and Rybach 2005). Thus, it is unlikely that pressure solution is the  
 320 viscous mechanism responsible for the **brittle-ductile transition**.

321 For a material that deforms by viscous creep according to Eq. 14.11, the  
 322 **compaction rate** (Wilkinson and Ashby 1975) is

$$\dot{\epsilon}_\phi = \frac{1}{\phi} \frac{d\phi}{dt} = -c_\sigma \frac{(1-\phi)^2}{(1-\phi^{1/n_\sigma})^{n_\sigma}} A |p_e|^{n_\sigma-1} p_e \approx -c_\sigma A |p_e|^{n_\sigma-1} p_e, \quad (14.16)$$

323 where the approximate form, which is adopted hereafter, applies in the small-  
 324 porosity limit. The geometric factor  $c_\sigma = n_\sigma^{-n_\sigma} (3/2)^{n_\sigma+1}$  follows rigorously only  
 325 for spherical pore geometry. At the level of accuracy required here, this geometric

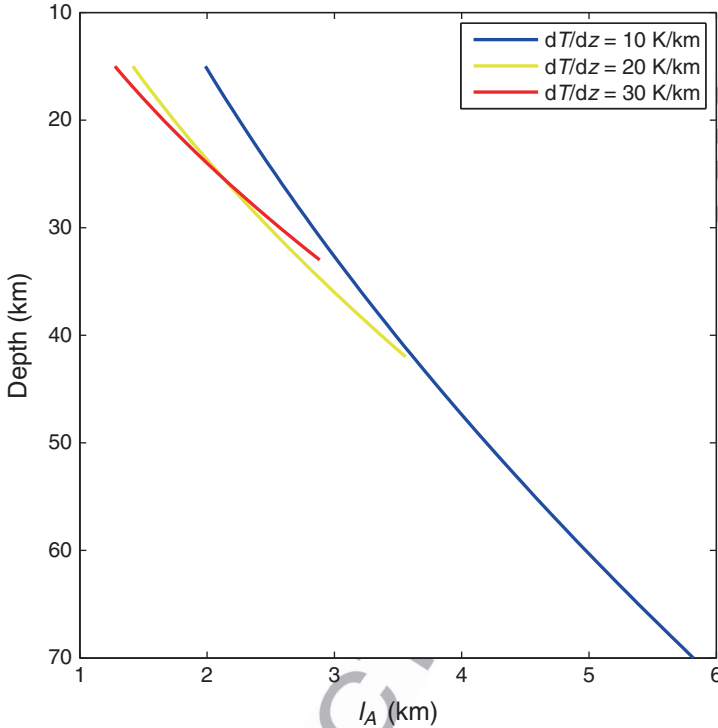


**Fig. 14.1** The viscous e-fold length  $l_A$  is the characteristic length scale for variation in the ductile rheology of the lower crust with depth due to thermal activation (Eq. 14.15). For a given stress, strain rates increase 10-fold over a depth interval  $\Delta z = 2.3 l_A$ . The viscous e-fold length is computed for the indicated geotherms, a reference temperature of 623 K at 15 km depth, and an activation energy of  $Q = 250$  kJ/mol. Experimentally determined activation energies for dislocation creep in silicate minerals are in the range 135–400 kJ/mol (e.g., Paterson and Luan 1990; Ranalli 1995). Variation within this range affects  $l_A$  by less than a factor of two

assumption is an unimportant source of variability. For the specific case of  $n_\sigma = 3$ ,  $c_\sigma = 3/16$ .

The dependence of the viscous compaction rate on effective pressure has a number of implications for compaction processes during metamorphism. Most notably the viscous mechanism cannot operate at the  $p_f = p_t$  condition generally assumed in metamorphic petrology. Thus, dilational strain, caused by a metamorphic reaction that initiates at  $p_f = p_t$ , must be accommodated by elastic mechanisms until the induced stresses become large enough to activate viscous or plastic deformation. As these elastic strains are insignificant, during this incipient stage metamorphism is effectively isochoric rather than isobaric.

The assumption that the viscous mechanism is non-linear is not essential to any subsequent argumentation; it is adopted because it is widely accepted and general. Relations for the special case of linear viscous rheology are obtained from the relations for the non-linear case by observing that, when  $n_\sigma = 1$ , viscosity is  $1/(3A)$ . Both

340 compaction and macroscopic shear deformation are accomplished by microscopic  
 341 shear. Thus, if a rock is simultaneously subject to both modes of deformation, then  
 342 they must be accommodated by the same microscopic mechanism. This mechanism is  
 343 determined by the largest of the stresses responsible for the deformation,  $|\Delta\sigma|$  or  $|p_c|$ ,  
 344 with the result that, if the stresses are of different magnitude, the viscous response to the  
 345 inferior stress is approximately linear and determined by effective viscosity resulting  
 346 from the deformation induced by the superior stress. Regardless of magnitude, far-field  
 347 tectonic stress facilitates compaction by lowering the effective viscosity of the solid  
 348 matrix (Tumarkina et al. 2011).

### 349 **14.2.2 Permeability**

350 Although the hydraulic permeability of rocks is extraordinarily variable, it is well  
 351 established from both theoretical studies and empirical observation (Wark and  
 352 Watson 1998; Xiao et al. 2006) that the permeability of a given rock will vary as  
 353 a strong function of its connected porosity. Typically, a power-law relationship is  
 354 assumed such that if the permeability is  $k_0$  at porosity  $\phi_0$ , then

no new paragraph

$$k = k_0(\phi/\phi_0)^{n_\phi} = c_\phi\phi^{n_\phi}. \quad (14.17)$$

355 In its second form, Eq. 14.17 separates the variability of permeability into a  
 356 component related to its porosity dependence and a coefficient,  $c_\phi$ , which is a  
 357 function of pore geometry and proportional to the square of the matrix grain size.  
 358 From analysis of in situ rock permeability, Neuzil (1994) shows that pore geometry  
 359 and grain size gives rise to variations in permeability that span eight orders of  
 360 magnitude, but that porosity dependence is approximately cubic. This cubic depen-  
 361 dence, i.e.,  $n_\phi = 3$ , is adopted here and is predicted from theory irrespective of  
 362 whether flow is intergranular or fracture controlled (Norton and Knapp 1977;  
 363 Gavrilenko and Gueguen 1993). Higher exponents are observed in rocks where  
 364 the degree of hydraulic connectivity varies strongly with porosity (Zhu et al. 1995;  
 365 Zhu et al. 1999).

### 366 **14.2.3 Porosity**

367 Given a steady source at depth, it is conceivable that crustal rocks could adjust their  
 368 permeability to accommodate this flux at lithostatic pressure (Connolly and  
 369 Thompson 1989). While such a model is problematic, as it implies rocks have no  
 370 strength, it provides the only basis for assuming that the lower crust has a tendency  
 371 to evolve towards a state with homogeneous permeability. Unfortunately, this  
 372 tenuous argument does not extend to porosity given that different lithologies may  
 373 have the same permeability with drastically different porosities (Neuzil 1994;

Thompson and Connolly 1990). Thus, the only certainty about lower crustal porosity is that it is spatially and temporally variable. An upper bound on lower crustal porosities of  $O(10^{-2})$  is provided by the sensitivity of geophysical measurements, but there is no lower bound. On the basis of isotopic diffusion profiles, Skelton et al. (2000) infer background porosities, i.e., the porosity in non-reactive metaphyllites about a metabasite undergoing devolatilization at greenschist facies conditions, in the range of  $\phi_0 \sim 10^{-3}$  to  $10^{-6}$ . These are consistent with grain scale porosities in the range  $10^{-3}$  to  $10^{-6}$  measured in exhumed metamorphic rocks (Norton and Knapp 1977). This variability has non-trivial consequences because, discounting the influence of phase changes on intrinsic material properties, the impact of metamorphic reactions on the mechanical properties of the crust is determined by the relative change in porosity via the constitutive relations for permeability (Eq. 14.17) and rheology (Eq. 14.16), e.g., an increase in porosity of  $10^{-3}$  has no significant influence on permeability if it occurs in rocks with an initial porosity of  $10^{-2}$ , but if the initial porosity is  $10^{-6}$ , permeability increases by nine orders of magnitude.

Hydraulically connected porosities of  $< O(10^{-2})$  may seem implausible to a reader familiar with percolation theory models of rock permeability (Gueguen and Palciauskas 1994); however such models assume static pore structure. In natural systems, experimental, theoretical, and numerical evidence suggests that textural equilibration may maintain hydraulic connectivity to vanishingly small porosities (Cheadle et al. 2004; cf., Holness and Siklos 2000 and Price et al. 2006). As remarked earlier (Sect. 14.1), the term porosity is used here to denote any hydraulically connected textural features (e.g., cracks) present on a spatial scale significantly less than the, as yet to be defined, compaction length scale. Thus, even if a percolation threshold is relevant to the expulsion process, porosity may take on any value between zero and unity. Evidence for high metamorphic fluid pressures, in combination with low fluid production rates, provides an indirect argument that these porosities are small at the onset of metamorphism. For example, theoretical porosity-permeability models (Connolly et al. 2009) imply that for  $O(1)$  mm grain size, the porosity necessary, to conduct a plausible  $O(10^{-13})$  m/s devolatilization-generated fluid flux (Connolly and Thompson 1989) at lithostatic pressure, is  $O(10^{-5})$ .

Whether rocks exist that have no hydraulically connected porosity is, to a certain degree, a metaphysical question. Viscous compaction may completely eliminate microcrack connectivity (Gratier et al. 2003; Tenthorey and Cox 2006), but, in texturally equilibrated rocks, grain-scale viscous compaction reduces porosity asymptotically with time. Similarly, chemical cementation and retrograde hydration require the ingress of a fluid phase and therefore are unlikely to completely eliminate porosity. Even seemingly pristine igneous rocks have detectable hydraulic connectivity (Norton and Knapp 1977). Regardless of whether rocks with no hydraulically connected porosity exist, it is certainly possible that devolatilization may occur in a setting in which the surrounding rocks have such low permeabilities that viscous dilational mechanisms become ineffective on the geological time scale. The compaction time scale, discussed subsequently (Sect. 14.5.2), can be used to assess when the viscous mechanism becomes ineffective. In this limit, elastic or

420 plastic dilational mechanisms must be responsible for fluid flow. Elastic and plastic  
421 mechanisms do not require finite hydraulic connectivity and are therefore also  
422 capable of explaining fluid flow into truly impermeable rocks (Connolly and  
423 Podladchikov 1998), but these mechanisms introduce complexities that are beyond  
424 the scope of this Chapter.

### 425 14.3 The Lower Crustal Hydrologic Regime

426 Conventional wisdom holds that continental crust can be divided into two hydro-  
427 logic regimes, an upper crustal regime in which fluid pressures are near hydrostatic  
428 and a lower crustal regime in which fluid pressures are lithostatic (Fig. 14.2a).  
429 Direct (Huenges et al. 1997) and geophysical observations (Zoback and Townend  
430 2001) confirm the existence of the upper regime and suggest that it can extend to  
431 depths of 10–15 km, while fluid inclusion data and deformation styles support the  
432 existence of the lower regime, at least during episodes of regional metamorphism  
433 (e.g., Etheridge et al. 1984; Sibson 1992; Cox 2005). The observation that fluid  
434 overpressures develop at a eustatic compaction front at ~3–4 km depth in many  
435 sedimentary basins suggests that compaction can establish a steady-state connec-  
436 tion between the hydrostatic and lithostatic regimes. However, this steady-state is  
437 only possible in conjunction with sedimentation, because sediment burial is neces-  
438 sary to compensate for upward propagation of the compaction front (Connolly and  
439 Podladchikov 2000). Given that steady burial is not a characteristic continental  
440 process, a steady-state connection between the hydrologic regimes is improbable.

441 In active metamorphic settings, the transition between hydraulic regimes can be  
442 explained by both the compacting and non-compacting limiting cases. In the  
443 compacting case, thermally activated viscous compaction reduces permeability to  
444 levels at which drainage to the upper crust cannot keep pace with expulsion and/or  
445 metamorphic fluid production. This scenario is the basis for the false notion that the  
446 transition to lithostatic fluid pressure is coincident with the brittle-ductile transition.  
447 Assuming hydrostatic fluid pressures are characteristic of the upper crust, at the  
448 brittle-ductile transition the effective pressure responsible for compaction is compar-  
449 able to the differential stress that drives tectonic deformation (Connolly and  
450 Podladchikov 2004). From Eqs. 14.11 to 14.16, the compaction rate at the transition  
451 is therefore comparable to the tectonic strain rate. Thus, for a tectonic strain rate of  
452  $10^{-15} \text{ s}^{-1}$ , compaction at the brittle-ductile transition requires  $2.3c_{\sigma}/\dot{\epsilon} \sim 388 \text{ My}$  to  
453 reduce porosity by an order of magnitude. As this time scale is greater than the time  
454 scale for heat-conduction limited metamorphism, compaction at the depth of the  
455 brittle-ductile transition is an ineffective means of regulating metamorphic fluid  
456 pressure, unless metamorphism is coeval with anomalously high rates of tectonic  
457 deformation. This generality applies to the expulsion process, but the healing of  
458 microcrack controlled permeability in shear zones is an indirect mechanism by  
459 which localized compaction at shallow crustal levels, and short time scales, may  
460 generate hydraulic seals (Gratier et al. 2003; Tenthorey and Cox 2006). These seals

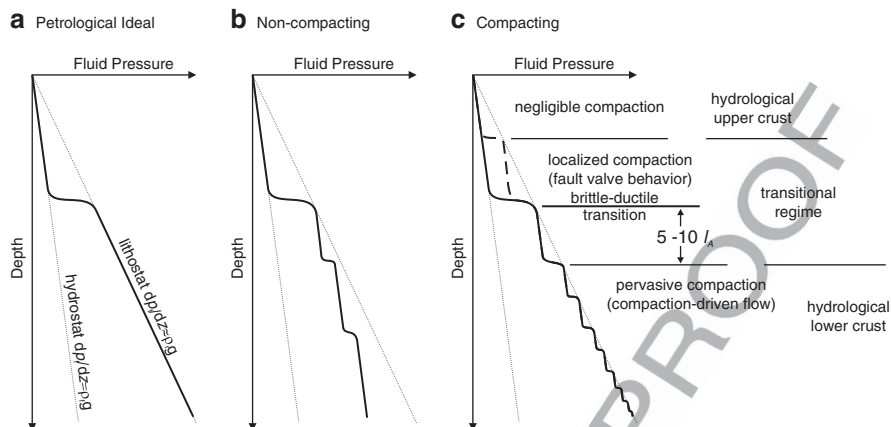


**Fig. 14.2** Three models for fluid pressure in the crust. The petrological lithostatic fluid pressure model (a) is hydrologically untenable unless permeability is uniform throughout the lower crust and the fluid originates from a steady sub-crustal source. In the non-compacting scenario (b) drainage of lower crustal rocks is limited by the least permeable horizon. In the absence of short-term effects related to fluid production, this horizon, i.e., **top-seal**, would mark the closest approach to lithostatic fluid pressure. Above this horizon fluid pressures would be near hydrostatic. While below the horizon fluid pressure would increase step wise across low permeability seals (Etheridge et al. 1984; Gold and Soter 1985; Hunt 1990; Powley 1990). The superposition of thermally activated compaction on the non-compacting scenario gives rise to three hydrologic regimes (c). An upper crustal regime in which faulting maintains such high permeabilities that negligible deviation from hydrostatic fluid pressure is adequate to drive fluid circulation (Zoback and Townend 2001) is limited at depth by the conditions at which **localized compaction** becomes an effective mechanism for sealing fault-generated permeability (Gratier et al. 2003; Tenthorey and Cox 2006). At greater depths, pervasive compaction and/or metamorphic fluid production may generate transient fluid overpressure that is periodically relieved by faulting (Sibson 1992). At the brittle-ductile transition (i.e., the base of the seismogenic zone) it is improbable that pervasive compaction can keep pace with metamorphic fluid production; thus the transitional hydrologic regime is likely to persist over an interval that extends  $\sim 10 l_A$  below the brittle-ductile transition. Beneath the transitional regime, **pervasive compaction** is capable of generating hydraulic seals and fluid, if present, is at near lithostatic pressure. Within this lower-most regime, fluid flow is truly compaction-driven. In the absence of fluid production, the tendency of both time and depth is to decrease the wavelength of the fluid pressure compartments resulting in a near-steady regime approximating the petrological ideal. Barring the possibility of a sub-crustal source, the flux in this near steady regime must decrease with depth. Thus the magnitude of the perturbation caused by metamorphic devolatilization to the lower crustal regime is dependent on its depth

may cause fluid overpressure to develop as consequence of local fluid production or deeper expulsion processes (Cox 2005). Viscous compaction rates increase by a factor of  $e$  with an increase in depth of  $\Delta z \sim l_A$ , thus the depth at which compaction operates pervasively on the metamorphic time scale must lie at least several viscous  $e$ -fold lengths (Fig. 14.1) below the **brittle-ductile transition**, but the exact depth is dependent on the rate of metamorphism.

In the non-compacting limit (Fig. 14.2b), lithostatic fluid pressure is generated when metamorphic fluid production overwhelms drainage capacity. A complication

469 in this scenario is that if fluid pressures are lithostatic throughout the lower crust,  
470 then either fluxes are uniform and vertical throughout the lower crust or permeabil-  
471 ity must be a function of flux rather than porosity. The physical absurdity of either  
472 case leads to the conclusion that a heterogeneous permeability structure is the only  
473 plausible model for the non-compacting limit. In this case (Fig. 14.2c), fluid  
474 pressures cannot be uniformly lithostatic, but approach lithostatic values at low-  
475 permeability seals (e.g., Etheridge et al. 1984). The resulting compartmentalized  
476 fluid pressure profile is identical to the **compartmentalization** observed in sedimentary  
477 basins (Hunt 1990; Powley 1990). Even in the non-compacting limit, brittle  
478 failure permits permeability to increase to accommodate vertical fluxes, but, given  
479 the variability of natural permeability with lithology, the permeability of a seal-  
480 forming lithology may be orders of magnitude lower than in the intervening rocks.  
481 If such seals exist, then, in the absence of metamorphic fluid production, the lower  
482 crust may achieve a quasi-steady state with near uniform vertical fluxes in which  
483 the closest approach to lithostatic fluid pressure occurs at the uppermost seal.  
484 Beneath each seal, Darcy's law requires that the fluid pressure gradient must be  
485 nearly hydrostatic, despite large absolute fluid pressures. The time scale for  
486 reaching this steady state is dictated by the high-permeability rocks, whereas the  
487 effective permeability of the lower crust is defined by the permeability of the top  
488 seal. As the vertical flux in this scenario must degrade with time, the number of  
489 effective seals must likewise decrease.

490 As a crustal model, the non-compacting limit has the virtue that it acknowledges  
491 the enormous variability of permeability with lithology and it has features that are  
492 consistent with both direct and indirect observation. In the former category, results  
493 from the Kola deep drilling project suggest the development of fluid compartment-  
494 talization at ~8 km depth within the crust (Zharikov et al. 2003). While in the latter  
495 category, the existence of permeable horizons with sublithostatic fluid pressure are  
496 essential to explain the lateral fluid flow so often inferred in metamorphic studies  
497 (Ferry and Gerdes 1998; Wing and Ferry 2007; Staude et al. 2009). Counter-  
498 intuitively, the non-compacting scenario is consistent with the idea that the  
499 brittle-ductile transition is coincident with the transition in crustal hydrologic  
500 regimes if faulting in the brittle domain is responsible for the high permeability  
501 of the upper crust (Zoback and Townend 2001).

502 Thermal activation of viscous compaction dictates the degree to which the  
503 compacting or non-compacting scenario is relevant to nature. As the non-  
504 compacting limit is broadly consistent with the upper crustal hydrologic regime, it  
505 is simplest to develop a conceptual model for the lower crust by considering how  
506 depth-dependent viscosity would perturb the non-compacting limit. The primary  
507 effect of depth-dependent viscosity would be to reduce the effective pressures  
508 sustained within, and therefore the vertical extent of, compartments with depth.  
509 Additionally, compaction would provide a source for fluxes, permitting pressuriza-  
510 tion of seals independently of the top seal. These two effects would lead to a decrease  
511 in the wavelength of fluid compartments with depth and lithostatically pressured  
512 seals throughout the lower crust, i.e., a pressure profile that would approximate the  
513 classical model of lithostatic fluid pressure at depth (Fig. 14.2c).

The absence of any uncontrived steady state for the lower crustal hydrologic regime poses a fundamental limitation to modeling metamorphic fluid flow in that the initial conditions for such models are unconstrained. Thus, by adjusting an arbitrary model parameter, such as the background fluid flux, the modeler has complete control on the impact of metamorphic fluid production on crustal fluid flow. This has the implication that forward modeling of metamorphic fluid flow has little predictive power and that hypothesis testing, based entirely upon modeling, is suspect. The utility of forward models is that they can be used to predict patterns. The comparison of these patterns with natural observations then provides a basis for inverting the parameters and the initial conditions of the metamorphic environments.

#### 14.4 Metamorphic Fluid Production and Dilational Strain

A first order constraint on metamorphic fluid production follows from the observation that between low and high metamorphic grades typical crustal rocks lose 5% of their mass as a consequence of devolatilization (Shaw 1956). For crustal thicknesses of  $l_c \sim 35\text{--}70$  km, this implies time-integrated fluxes of the order

$$\hat{q} = \frac{w\rho_r l_c}{\rho_f} \sim O(10^4)\text{m} \quad (14.18)$$

where  $w$  is the weight fraction of the volatiles released during metamorphism. This estimate is comparable to, or greater than, integrated fluxes derived from field studies (e.g., Ferry 1994; Skelton 1996; Wing and Ferry 2007; Staude et al. 2009) suggesting that, at least from a mass balance perspective, there is no necessity to invoke convection cells or exotic fluid sources to explain typical metamorphic fluxes. Introducing the assumptions that fluid expulsion keeps pace with metamorphic fluid production and that the duration of metamorphism is dictated by the heat conduction time scale ( $\tau_{\text{met}} \sim l_c^2/\kappa$ , where  $\kappa$  is thermal diffusivity,  $O(10^{-6})$  m<sup>2</sup>/s for crustal rocks), time-averaged fluxes are of the order

$$\bar{q} = \frac{w\rho_r \kappa}{\rho_f l_c} \sim O(10^{-12})\text{m/s}. \quad (14.19)$$

By introducing an additional assumption about the pressure gradient responsible for the average flux, Darcy's law can be inverted for time-averaged permeability (Ingebritsen and Manning 1999). The simplicity of this logic is seductive, but because metamorphic fluxes are dynamic, such averages are misleading. For example, Fulton et al. (2009) reject the contention of Ague et al. (1998) that dehydration generated fluid overpressures may trigger faulting. The fallacy of the argumentation being that, by definition, the average permeability is the permeability necessary to accommodate metamorphic fluxes at lithostatic pressure, thus it is unsurprising that a dynamic metamorphic flux is inadequate to generate

no new paragraph

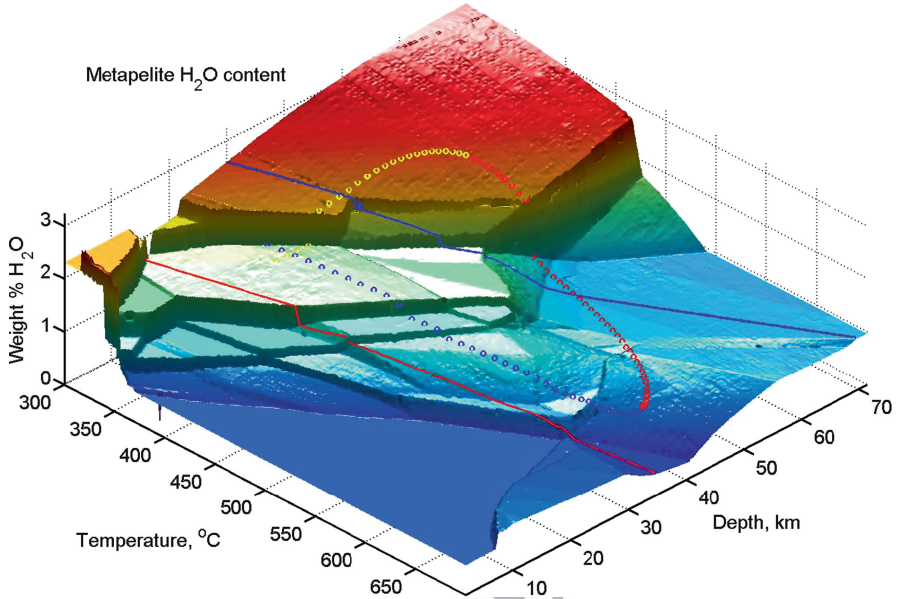


**Fig. 14.3** Water-content for an average pelitic sediment composition (Plank and Langmuir 1998) as a function of temperature and pressure, computed assuming equilibrium with a pure H<sub>2</sub>O fluid. Red and blue lines indicate hot (20°C/km) and cold (10°C/km) metamorphic geotherms. The increase in water-content at temperatures > 600°C is due to melting that occurs because the model assumes water-saturation. This melting does not occur if the water released by low temperature processes is expelled (Modified from Connolly (2010)).

548 overpressures if this permeability is assumed as an initial condition. From the point  
 549 of view of understanding dynamic flow, average permeability has no utility unless  
 550 permeability is a static property. However, it would be fortuitous if this static  
 551 permeability were exactly the permeability necessary to conduct metamorphic  
 552 fluxes at lithostatic pressure. Thus, the pertinent issue to understanding lower  
 553 crustal fluid flow is not the average permeability of the lower crust, but rather the  
 554 background permeability that characterizes the environment prior to the onset of the  
 555 flow perturbation of interest.

556 To illustrate the variability of metamorphic fluid production, consider equilib-  
 557 rium dehydration of a pelitic rock (Fig. 14.3). In the closed system limit, the  
 558 classical lithostatic fluid pressure model requires that volume changes associated  
 559 with devolatilization must be instantaneous. In the context of this model, the  
 560 instantaneous dilational strain is a function of pressure and temperature and can  
 561 be decomposed into components representing fluid and solid volumetric production  
 562 rates (Fig. 14.4). The rates are broadly consistent with the expectation that meta-  
 563 morphic devolatilization is associated with a reduction in solid volume, but an  
 564 increase in total volume; a behavior that would increase fluid pressure and drive  
 565 dilational deformation in real systems. If hydrofracture provides an instantaneous  
 566 dilational mechanism then the equilibrium model can be realized for the general  
 567 case. Exceptions to this generality occur at the extremes of the metamorphic

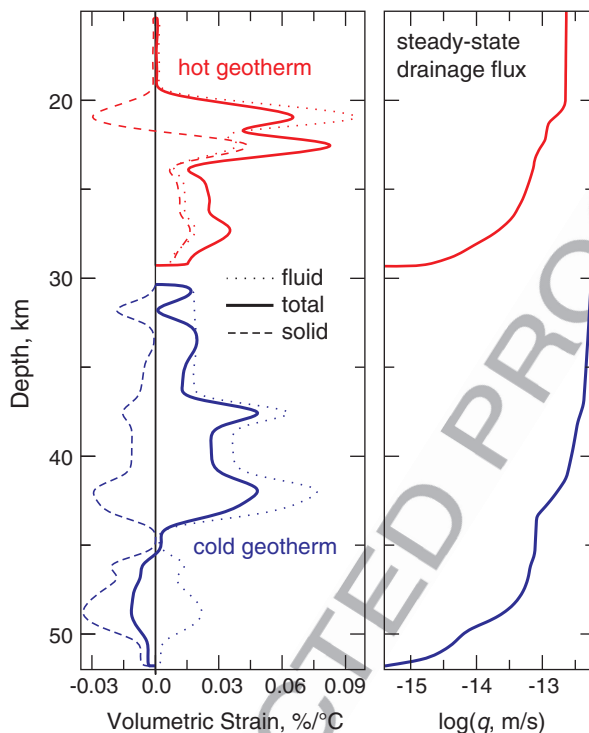


**Fig. 14.4** Dehydration induced, isobaric strain, and steady-state fluid fluxes as a function of depth for the metamorphic model depicted in Fig. 14.3. The strain is resolved into the components due to fluid and solid production and corrected for the effect of thermal expansivity. Fluid and solid production rates are the product of the corresponding component of the isobaric strain multiplied by the metamorphic heating rate. The steady-state drainage flux  $q$  is the vertically integrated fluid production rate computed for a heating rate of  $3^\circ\text{C}/\text{My}$ . This is the flux required for drainage to balance fluid production. For the hot geotherm, the curves are terminated at the onset of melting because the melting process is dependent on the dynamics of fluid expulsion (Modified from Connolly (2010)).

spectrum, i.e., at low temperature and high pressure or high temperature and low pressure. In the former case, the net volume change may be negative, an effect that would generate sub-lithostatic fluid pressures and therefore cause reaction rates to be limited by relatively slow viscous compaction mechanisms. In contrast, along high geothermal gradients the solid volume may increase (Fig. 14.4) during devolatilization requiring a more complex dilational deformation process than the hydrofracture mechanism assumed here.

Under the assumption that fluids are expelled upwards as rapidly as they are produced, metamorphic fluxes are the vertically integrated fluid production rate, i.e., the component of the dilational strain rate attributed to fluid generation. Taking a heating rate of  $3\text{ K}/\text{My}$  and assuming consistent heat-conduction controlled metamorphism (England and Thompson 1984), fluid fluxes estimated in this way for both cool and warm geothermal conditions are comparable to the average flux deduced earlier (Fig. 14.4). However, the more detailed model illustrates that fluxes

582 must vary by orders of magnitude with depth. These fluxes place an upper bound on  
583 the **effective permeability** of the lower crust, because it would be impossible to  
584 generate elevated fluid pressure at a higher permeability. Unfortunately, there is  
585 little reason to expect that background permeabilities will be conveniently close to  
586 this upper bound, although they may well correlate with rates of metamorphism.  
587 This latter issue is topical because recent studies (Oliver et al. 2000; Dewey 2005;  
588 Ague and Baxter 2007; Warren et al. 2011) suggest that at least some episodes of  
589 regional metamorphism occur on time scales one to two orders of magnitude shorter  
590 than implied by the heat conduction time scale.

## 591 **14.5 Fluid Flow in Compacting Media: **Porosity Waves****

592 Evidence that metamorphic devolatilization occurs at elevated fluid pressure leaves  
593 little doubt that devolatilization perturbs the pre-metamorphic hydrologic regime. In  
594 rigid rock, the dilational strain required for reaction progress is eliminated if the fluid  
595 is simultaneously drained by hydraulic diffusion. However, if the rocks initially  
596 contain fluid at or near lithostatic pressure, then, from Darcy's law, the fluid pressure  
597 gradient required for this drainage must be supralithostatic and therefore inconsis-  
598 tent with the existence of lithostatic fluid pressure during metamorphism. If the  
599 definition of rigid is relaxed to allow for brittle failure at insignificant overpressure,  
600 the coupling between reaction rate and pressure is eliminated, but so too are the fluid  
601 overpressures that would be capable of explaining increased fluid drainage. Thus,  
602 without compaction, the effect of brittle failure is to generate a horizon of elevated  
603 porosity, filled by near lithostatically pressured fluid, sandwiched between relatively  
604 impermeable unreacted rocks. The horizon is analogous to a wet sponge in that it  
605 releases fluid only if it is squeezed. The weight of the overlying rocks acts as the  
606 agent for squeezing by, what has been argued here to be, predominantly, viscous  
607 compaction. The rate at which the fluid is drained is fundamentally limited by the  
608 permeability of the overlying rocks, but because these rocks are also deformable this  
609 permeability is dynamic. As noted earlier, the peculiar feature of fluid flow in this  
610 scenario is that it occurs in waves of fluid-filled porosity. An idealized 1-d, constant  
611 viscosity, model is employed here to explain why these waves form, after which the  
612 model is extended to account for more complex rheology and multidimensional  
613 effects.

### 614 **14.5.1 Porosity Waves in Viscous Rock, Why?**

615 For simplicity consider a constant volume devolatilization reaction that initiates at  
616 depth within an otherwise uniform rock subject to some small background fluid flux  
617  $q_0$  (Fig. 14.5). Initially, since the reaction is isochoric it does not perturb the  
618 background flux, but it does increase the porosity from  $\phi_0$  to  $\phi_1$  by reducing the  
619 solid volume. This porosity change increases the permeability within the reacted

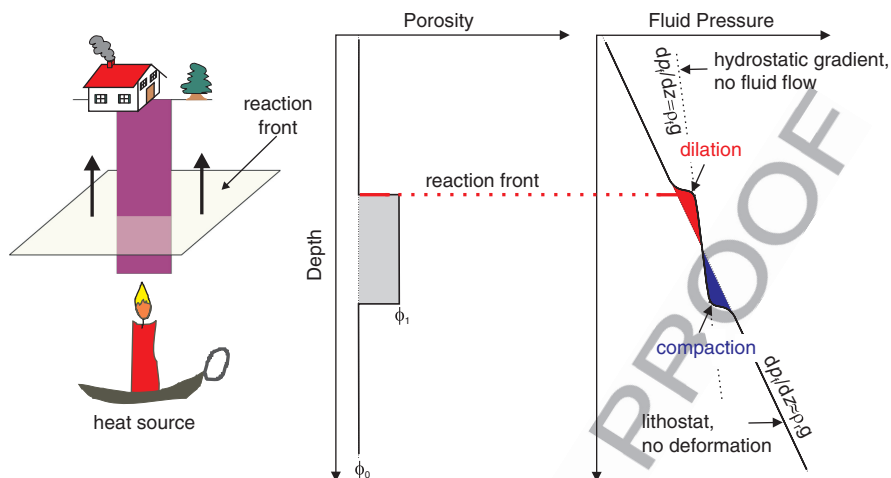


**Fig. 14.5** Conceptual model of an isochoric metamorphic devolatilization reaction. The unreacted rock has porosity  $\phi_0$  and conducts the flux  $q_0$ . The reaction leaves a region of elevated porosity  $\phi_1$  in its wake. This high porosity region has a permeability  $(\phi_1/\phi_0)^3$  times greater than in the unreacted rock (for  $n_\phi = 3$  in Eq. 14.17). Because there are no dilational effects associated with an isochoric reaction, the flux in the permeable reacted region must initially be the same as the background flux. For this to be true Darcy's law requires that the effective pressure gradient in the reacted rocks must be  $\Delta p g / (\phi_1/\phi_0)^3$ ; thus a factor of 2 increase in porosity reduces the fluid pressure gradient to within 12.5% of the hydrostatic gradient. As the vertical extent of the reacted rocks becomes larger with time, this condition causes finite effective pressure anomalies that lead to fluid expulsion. Non-isochoric reactions lead to a similar scenario, but with asymmetric pressure anomalies (Connolly 1997) (Modified from Connolly (2010))

rocks by a factor of  $(\phi_1/\phi_0)^3$  (for  $n_\phi = 3$  in Eq. 14.17). From Darcy's law, if fluid  
 620 flux is constant then an increase in permeability must be compensated by a  
 621 reduction in the fluid pressure gradient. Thus, an order of magnitude increase in  
 622 permeability is sufficient to cause the fluid pressure gradient to relax to essentially  
 623 hydrostatic values within the reacted rock. In turn, this relaxation gives rise to an  
 624 effective pressure gradient such that pore fluids are overpressured above the center  
 625 of the reacted zone and underpressured below it (Fig. 14.5). These pressure  
 626 anomalies induce transient perturbations to the fluid flux above and below the  
 627 reacted zone, but because the anomalies are antisymmetric there is no net drainage  
 628 of fluid from the reacted layer as long as deformation is insignificant. However, the  
 629 magnitude of the pressure anomalies must grow in proportion to the vertical extent  
 630 of the reacted rocks with the result that deformation becomes inevitable. This  
 631 deformation is manifest as compaction at the base of the reacted rocks and dilation  
 632 at their top and has the effect of propagating the reaction-generated porosity upward  
 633 (Fig. 14.6a). If the rate of propagation is high enough, then this mechanism can  
 634 generate an isolated domain, or wave, of porosity that separates from the reaction  
 635 front. Alternatively if the domain moves too slowly to detach from the source a  
 636 wave train develops. The isolated wave and wave train correspond to steady-state  
 637 solitary (Richter and McKenzie 1984; Barcion and Richter 1986) and periodic  
 638 (Sumita et al. 1996; Connolly and Podladchikov 1998) wave solutions of the  
 639

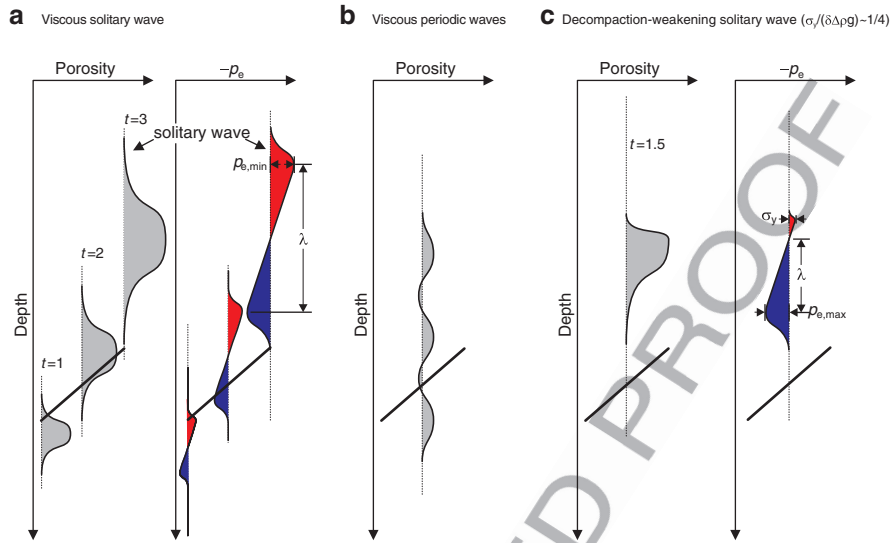


**Fig. 14.6** Time evolution of reaction-generated porosity and fluid overpressure,  $p_f - p$ , profiles in a viscous solid matrix. For each profile the baseline is indicated by a vertical dotted line that corresponds to the background porosity,  $\phi_0$ , or zero overpressure. In the symmetric viscous case (a), the magnitude of the fluid pressure anomalies within the reaction-generated porosity is proportional to the vertical extent of the high porosity. Thus, the anomalies grow as the reaction front advances upward until they become large enough to cause significant deformation. Thereafter, compaction at the base of the high porosity region squeezes fluid upward to the upper portion of the high porosity region where it is accommodated by dilational deformation. This process has the effect of propagating the reaction-generated porosity upward. The high porosity region detaches from the source when the compaction rate at the base becomes comparable to the fluid production rate giving rise to a solitary wave that propagates independently of its source (Richter and McKenzie 1984; Connolly 1997). For the solitary wave to be stable it must propagate with speed  $v_\phi > n_\phi v_0$  (Appendix, Eq. 14.54). If the source is too weak to sustain a wave with this speed then a periodic wave train forms that is unable to separate from the source (b). These waves dissipate if the source is exhausted. If the fluid overpressures are large enough to induce embrittlement, decompaction becomes viscoplastic (c), but the compaction remains viscous. In this case, the lower portion of the solitary wave is unchanged from the symmetric viscous case, but hydrofracturing acts as homeostat that regulates the overpressures in the upper portion of the wave. The scenarios depicted here assume that the speed at which the reaction front propagates upward is not much greater than the speed of fluid flow  $v_0$  through the unperturbed matrix, in the alternative, fast devolatilization scenario (Sect. 14.5.3) waves detach from the source only after the cessation of devolatilization

640 equations that govern two-phase flow in an infinite viscous matrix (Fig. 14.6b and  
 641 Appendix). In the case of the solitary wave solution, the steady state consists of a  
 642 single isolated wave that propagates without dissipating. Because of its solitary  
 643 character, this steady state can plausibly be realized in nature and has been verified  
 644 in analog experiments (Scott et al. 1986). Additionally, numerical experiments have  
 645 shown that solitary waves are resistant to perturbations, e.g., if two waves collide  
 646 they regain their initial form after the collision (Richter and McKenzie 1984; Scott  
 647 and Stevenson 1986). In contrast, the periodic steady state consists of an infinite

wave train, which cannot be realized in nature. Thus, although a finite periodic wave train, in close proximity to the infinite steady state, may develop in response to a fluid source, once the source is exhausted the finite wave train will spread and dissipate to smooth flow.

#### 14.5.1.1 Why Don't Solitary Waves Dissipate?

It is natural to wonder why steady-state wave solutions exist at all. The origin of the phenomenon is the non-linear relation between porosity and permeability (e.g., Eq. 14.17) that permits flow perturbations to grow into shocks that propagate more rapidly than the fluid flows by hydraulic diffusion (Spiegelman 1993). This phenomenon is most easily explained for a matrix with no strength (i.e., the classical metamorphic model) in which case fluid pressure is lithostatic and fluid flux and velocity are solely a function of porosity. Consider then a situation in which a region with a large flux ( $\mathbf{q}_1 = \mathbf{v}_1\phi_1$ ) is overlain by a region with a small flux ( $\mathbf{q}_0 = \mathbf{v}_0\phi_0$ ) and that the regions are, initially, connected by a region in which the porosity decreases upward (Fig. 14.7a). From Eqs. 14.9 to 14.17, in terms of the fluid velocity in the low porosity region, the fluid velocity at any other porosity is

$$\mathbf{v} = \mathbf{v}_0(\phi/\phi_0)^{n_\phi-1}. \quad (14.20)$$

At any point where the porosity gradient is finite and decreases in the direction of flow, the divergence of the flux (i.e., the difference between the flux into and out of an infinitesimal volume) is also finite. This divergence must be manifest by an increase in porosity, i.e., dilational strain, which leads to a steepening of the porosity gradient and, ultimately, the formation of a porosity shock (i.e., a self-propagating step in the porosity profile, Fig. 14.7b). Because the shock is moving more rapidly than the fluid in front of shock, in a reference frame that moves with the shock, the flux from the unperturbed matrix must be directed toward the shock. Consequently, as the shock propagates it gains fluid volume at the rate  $q_1 - q_0$  from the low porosity region. As the porosity behind the shock is constant, conservation of the fluid volume requires that the shock velocity satisfies

$$\mathbf{v}_\phi = (\mathbf{q}_1 - \mathbf{q}_0)/(\phi_1 - \phi_0), \quad (14.21)$$

or, making use of Eq. 14.20,

$$\mathbf{v}_\phi = \mathbf{v}_0(1 - (\phi_0/\phi_1)^{n_\phi})/(\phi_1/\phi_0 - 1). \quad (14.22)$$

From Eq. 14.22, the smallest discrepancy between the velocity of the shock, and that of the fluid behind the shock, occurs in the limit that the shock is small, i.e.,  $\phi_1 \rightarrow \phi_0$ . The solitary porosity wave represents a steady state in which the finite strength of the matrix balances the tendency of fluid flow to steepen the porosity profile. Although the solitary wave is more complex than the simple shock, the

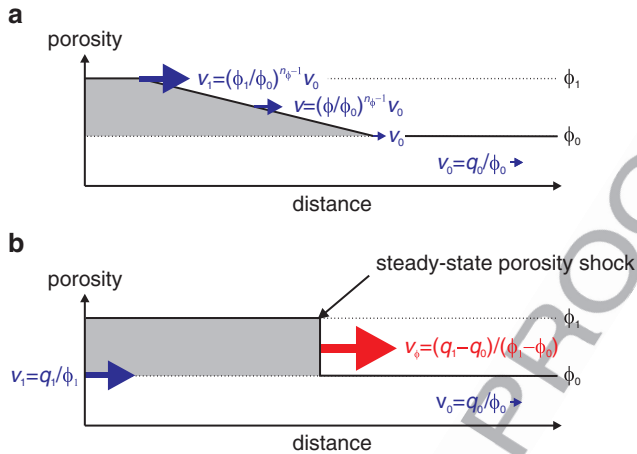


**Fig. 14.7** Formation of a porosity shock during fluid flow through an inviscid matrix (i.e., the classical metamorphic model). If the matrix is inviscid, then fluid pressure must be lithostatic and fluid velocity is solely a function of porosity. Consequently, if porosity decreases in the direction of flow, fluid in the high porosity direction catches up to the fluid in the low porosity region. This process increases the porosity gradient until it becomes infinite. At which point, the resulting step in the porosity profile corresponds to a porosity shock. In a reference frame that moves with the shock, the fluid flux from the unperturbed matrix is negative; thus the shock must travel more rapidly than the fluid behind it (Eq. 14.22). The minimum discrepancy between the fluid and shock velocities occurs when the porosity behind the shock is only infinitesimally larger than the background value. In this case, the velocity of the shock is  $n_\phi v_0$ , and corresponds to the minimum velocity at which the solitary wave solution is stable in a matrix with a finite viscosity (Appendix, Eq. 14.54)

681 solitary wave must have the same properties as the simple shock at the conditions  
 682 where it connects to the unperturbed porosity. At this point the fluid velocity is  $v_0$   
 683 and, from Eq. 14.22, the velocity of the simple shock is  $n_\phi v_0$ . Thus, a requirement  
 684 for the existence of steady-state solitary porosity waves is that they move  $\sim n_\phi$   
 685 times faster than the flow through the unperturbed matrix (Appendix, Eq. 14.54). As  
 686 in the simple shock, the solitary wave catches up with fluid flow through the  
 687 background porosity with the consequence that a geochemical signal from the  
 688 wave source may become diluted with time. The magnitude of this effect can be  
 689 quantified (Spiegelman and Elliott 1993), but it is insignificant for large amplitude  
 690 waves, i.e.,  $\phi_{\max} \gg \phi_0$ .

### 691 **14.5.2 One-Dimensional Isothermal Waves: How Big,** 692 **How Fast, and How Much?**

693 In the limit of a small perturbation to steady fluid flow through a uniform fluid-filled  
 694 porosity, compaction phenomena develop on a natural length scale known as the  
 695 **viscous compaction length** (McKenzie 1984). For a power-law viscous matrix this  
 696 scale (Appendix, Eq. 14.63) is

$$\delta = \phi_0^{\frac{n_\phi - 1}{n_\sigma + 1}} \sqrt[n_\sigma]{\left(\frac{2}{n_\sigma + 1}\right)^{n_\sigma} \frac{c_\phi}{c_\sigma A \mu (\Delta \rho g)^{n_\sigma - 1}}}, \quad (14.23)$$

no new paragraph

The compaction length is an estimate of the depth interval over which the matrix can sustain a non-lithostatic pressure gradient and, as such, it is unsurprising that it increases both with the strength ( $\propto 1/A$ , Eq. 14.16) of the matrix and the ease with which fluid flows through it ( $\propto c_\phi/\mu$ ). The speed of fluid flow at lithostatic fluid pressure through the unperturbed matrix,  $v_0 \approx c_\phi \phi_0^{n_\phi - 1} \Delta \rho g / \mu$  (Eqs. 14.4 and 14.9), provides a natural scale for the speed of compaction processes. From this speed the compaction time scale ( $\delta/v_0$ ) is

$$\tau = \phi_0^{\frac{n_\sigma(1-n_\phi)}{n_\sigma+1}} \sqrt[n_\sigma]{\left(\frac{\mu}{c_\phi(\Delta \rho g)^2}\right)^{n_\sigma} / A}, \quad (14.24)$$

no new paragraph

The **compaction scales** given by Eqs. 14.23 and 14.24 separate the porosity  $\phi_0$  of the fluid-rock aggregate from material properties ( $A$ ,  $\Delta \rho$ ,  $\mu$ ,  $c_\phi$ ) that are, at least in principle, measurable quantities. In metamorphic problems this porosity is an unknown property of the initial state. The challenge presented by metamorphic fluid expulsion is to find observations that constrain the compaction scales and thereby this initial state. Because the compaction scales are formulated in terms of the initial state they represent, for  $n_\sigma > 1$  and  $n_\phi > 1$ , a lower bound on the length scale and an upper bound on the time scale for fluid expulsion.

Given the uncertainties in the material properties involved in the compaction scales, it may be preferable to use observational constraints to infer the magnitudes of these scales. To this end, **background flux**  $q_0$ , which is presumably less than the time-averaged metamorphic flux, provides a useful proxy for the hydraulic material properties. Taking the observations of Young and Rumble (1993), van Haren et al. (1996), and Graham et al. (1998) to be indicative of compaction time scales  $O(10^4)$  y at amphibolite facies conditions ( $T = 773 - 923$  K), in conjunction with a plausible estimate for  $v_0 = q_0/\phi_0$  of  $10^{-10}$  m/s, the compaction length ( $\delta = \tau v_0$ ) consistent with these observations is 31 m. Clearly, it would be preferable to have direct observational constraints on the compaction length scale, as might be provided by variation in the pressures ( $O(2\delta\Delta\rho g)$ ) recorded by syn-metamorphic fluid inclusions or, as discussed subsequently, by the length scale ( $O(\delta)$ ) for lateral fluid flow. However, taken at face value, an  $O(10^4)$  y time scale and an  $O(10^2)$  m length scale implies a viscous rheology roughly three orders of magnitude weaker than given by Eq. 14.14 for tectonic strain rates  $O(10^{-15})$  s $^{-1}$ . A discrepancy of this magnitude can be explained if fluid expulsion is contemporaneous with pulses of intense tectonic deformation that lower the effective viscosity of the crust; an explanation consistent with a **non-uniformitarian model** of deformation and metamorphism (Oliver et al. 2000; Dewey 2005; Ague and Baxter 2007).

There is no fundamental principle that dictates a steady-state balance between metamorphic fluid production and transport, but for the range of conditions

733 investigated by numerical simulations of metamorphic compaction-driven fluid  
 734 flow (Connolly 1997; Connolly 2010) such a balance does develop locally. A  
 735 requirement for this balance is that the time-averaged flux associated with the  
 736 passage of a wave must be greater than or equal to the vertically integrated  
 737 production,  $\bar{q}$ , because a wave with  $q_e < \bar{q}$  would be unable to separate from its  
 738 source. This time-averaged flux is

$$q_e = \frac{v_\phi}{\lambda} V_e^{1d} \quad (14.25)$$

739 where  $\lambda$  and  $v_\phi$  are the length and speed of the wave, and

$$V_e^{1d} = \int_{-\lambda/2}^{\lambda/2} (\phi - \phi_0) dz \quad (14.26)$$

740 is the fluid volume associated with the wave, which in one dimension has units of  
 741 length. If  $q_e > \bar{q}$ , then the waves must be separated by a depth interval of

← no new paragraph  $\Delta z = \lambda(q_e/\bar{q} - 1)$

742 In 1-d numerical simulations, the transient dynamics of wave separation are such  
 743 that  $q_e/\bar{q}$  is typically  $< 2$  (Connolly 1997). This result suggests that, to a first  
 744 approximation, the properties of waves expected in metamorphic environments  
 745 can be predicted from the steady-state solitary wave solution to the compaction  
 746 equations (Fig. 14.8). The **solitary wave solution** does not exist for values of  
 747  $q_e/q_0 < 2$  (Appendix, Eq. 14.53), thus weak sources, or strong background fluxes,  
 748 will generate periodic waves that degenerate to uniform flow once the source is  
 749 exhausted. **Periodic solutions** to the compaction equations exist for all conditions;  
 750 however numerical (Richter and McKenzie 1984; Scott and Stevenson 1986;  
 751 Wiggins and Spiegelman 1995; Connolly 1997) and analog (Scott et al. 1986)  
 752 simulations suggest that the solitary wave solution is the stable solution whenever  
 753 it is a possible solution. The reason for this stability is unclear, but is most probably  
 754 related to the fact that the solitary wave is the more effective expulsion mechanism  
 755 and therefore maximizes the rate of dissipation of gravitational potential energy.

756 Because the matrix recovers to the background porosity asymptotically in a  
 757 steady-state solitary wave (for  $n_\sigma \geq 1$ ), the wavelength of the true steady state is  
 758 infinite (Appendix, Eq. 14.59). For practical purposes, it is desirable to define an  
 759 effective wavelength, which defines the extent of the wave that includes the bulk of  
 760 the anomalous porosity. Two non-arbitrary measures of **wavelength** are the distance  
 761 between the points of minimum and maximum effective pressure ( $\lambda$ ) and twice  
 762 the second moment of the porosity distribution within the wave ( $\lambda_1$ , Fig. 14.8c),  
 763 the former value being roughly half the latter. Comparison of the excess volume  
 764 obtained by integrating the porosity over these intervals to the total excess volume  
 765 obtained by integrating over infinite space (dashed curve, Fig. 14.8d) shows that,

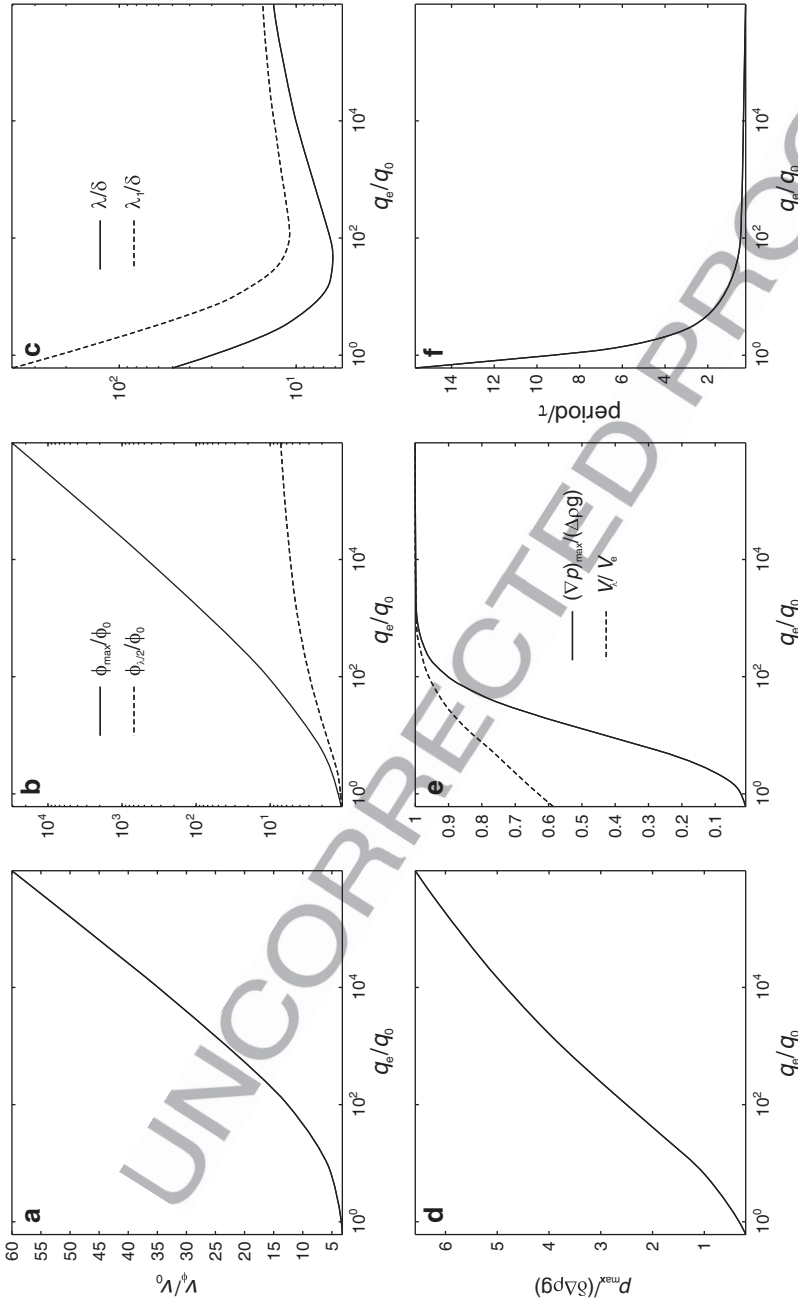


**Fig. 14.8** Steady-state 1-d solitary wave properties (for  $n_\sigma = n_\phi = 3$ ) as a function of the excess fluid flux  $q_e$ , which is the time-averaged flux associated with the passage of a porosity wave estimated as the product of the wave period and its excess volume. The power law exponent does not influence the speed-amplitude relation, but wavelength increases inversely with  $n_\sigma$ . **(a)** Wave speed,  $v_\phi$ . **(b)** Maximum porosity  $\phi_{\max}$ , and porosity at the depth of maximum effective pressure within a wave (Fig. 14.6a). **(c)** Two measures of the spatial extent of solitary waves:  $\lambda$  is the depth interval between the minimum and maximum effective pressure (Fig. 14.6a), and  $\lambda_1$  is the second moment of the porosity distribution. **(d)** Maximum effective pressure within the wave. **(e)** Maximum effective pressure gradient ( $\phi = \phi_{\max}$ ,  $P_e = 0$ ) and the fraction of the total excess volume of the wave that occurs within the depth interval  $\pm \lambda/2$  around  $\phi_{\max}$ . **(f)** Wave period,  $\lambda/v_\phi$ .

766 even at the minimum  $q_e$  for solitary wave stability,  $>80\%$  of the porosity of a wave  
 767 occurs within a distance of  $\pm \lambda/2$  from its center. Accordingly,  $\lambda$  is adopted here as  
 768 the measure of wavelength rather than the more conservative measure  $\lambda_1$ . The  
 769 solitary **wave period**,  $\lambda/v_\phi$ , is the time required for a wave to travel its wavelength.

770 To illustrate the quantitative implications of the solitary wave solution, consider  
 771 the initial condition  $\phi_0 = 10^{-4}$ ,  $q_0 = 10^{-14}$  m/s,  $\tau = 10$  ky, and  $\delta = 31$  m, which,  
 772 as discussed previously, is chosen to be consistent with the timing of fluid-rock  
 773 interaction during amphibolite facies metamorphism (Young and Rumble 1993;  
 774 van Haren et al. 1996; and Graham et al. 1998). From this condition, and the  
 775 properties of the solitary wave steady state (Fig. 14.8), the waves required to  
 776 conduct a typical metamorphic flux  $\bar{q} = 10^{-12}$  m/s (i.e.,  $q_e/q_0 = \bar{q}/q_0 = 10^2$ ) have  
 777  $\lambda = 200$  m,  $\phi_{\max} = 1.0 \cdot 10^{-3}$ , travel at  $v_\phi = 39$  m/ky, and are associated with fluid  
 778 pressure anomalies of 1.4 MPa. These pressure anomalies are small enough that a  
 779 viscous dilational mechanism for wave propagation is plausible. The sensitivity of  
 780 this result is demonstrated by considering the effect increasing  $\bar{q}$  to  $10^{-10}$  m/s,  
 781 which is consistent with the rate for Dalradian regional metamorphism inferred by  
 782 Ague and Baxter 2007. For this increased flux,  $\lambda = 320$  m,  $\phi_{\max} = 55 \cdot 10^{-3}$ ,  
 783  $v_\phi = 110$  m/ky, and  $p_{\max} = 2.9$  MPa; the most prominent difference being the  
 784 large increase in porosity.

### 785 **14.5.3 Fast Versus Slow Devolatilization and Complex Fluid** 786 **Sources**

787 The knife-edge sharp, constant volume, devolatilization reaction used so far for  
 788 purposes of illustration may seem unrealistic, but it captures the essence of the fluid  
 789 expulsion problem, which is not how fluid is released, but rather how it escapes. The  
 790 key to predicting the waves that are likely to evolve in response to more complex  
 791 devolatilization processes is to obtain plausible estimates for both the background  
 792 flux that the system is capable of accommodating without appreciable dilational  
 793 deformation and the excess flux generated by devolatilization that must be  
 794 accommodated by porosity waves.

795 The relationships between porosity wave speed and excess flux (Fig. 14.8a) and  
 796 between excess flux and wave amplitude (Fig. 14.8b) indicate that extraordinarily  
 797 large porosities are required to generate waves that travel more than two orders of  
 798 magnitude faster than the speed of the fluid flow in the unperturbed matrix. As the  
 799 analytical formulation ignores large porosity effects that lead to a further weaken-  
 800 ing of the dependence of speed on amplitude, it is reasonable to conclude that if  
 801 natural porosity waves exist, then they do not propagate at speeds  $\gg v_0$ . Given  
 802 that a porosity wave can only escape from a devolatilization reaction front if it  
 803 travels faster than the front, these considerations imply that the wave nucleation  
 804 scenario outlined in Sect. 14.5.1 represents the limiting case of **slow devolati-**  
 805 **lization**, wherein the devolatilization front propagates at speeds that are **not much**

~~greater than~~  $v_0$ . In the alternative, **fast devolatilization** scenario, devolatilization generates a high porosity source region. Porosity waves cannot escape from this source until lithological heterogeneity or geodynamic factors hinder the advance of the devolatilization front. If it is assumed that the material properties of the reacted and unreacted rocks do not differ significantly, then the porosity increase within the source region decreases the time scale for intra-source fluid expulsion (Eq. 14.24). This increase in efficiency has the consequence that the excess flux delivered to the upper boundary of the source region is independent of the processes in the unreacted rocks, which compact on a longer time scale. If the porosity,  $\phi_1$ , within the source is  $\gg \phi_0$ , then this excess flux is  $\sim q_0(\phi_1/\phi_0)^{n_\phi}$  and the waves that ultimately evolve from the source can be expected to carry a flux that is greater than, but comparable to this flux. Spiegelman (1993) demonstrated that in the waves which nucleate at the boundary between the source and unreacted rocks are not true solitary waves. However, for large porosity contrasts, i.e.,  $\phi_1 \gg \phi_0$ , the distinction is not important and is diminished still further in models that account for the elastic compressibility of the fluid (Connolly and Podladchikov 1998).

The dehydration model presented earlier suggests that in nature devolatilization ~~in nature~~ may occur by many reactions simultaneously over depth intervals of several kilometers (Fig. 14.3). The increase in porosity caused by reactions increases the compaction length within such an interval, an effect that will tend to blur the influence of individual reactions. Thus the characteristics of waves that would evolve above such an interval can be anticipated by equating the excess flux to either the vertically integrated fluid production in the slow devolatilization limit, or to  $q_0(\phi_1/\phi_0)^{n_\phi}$  in the fast limit.

A reaction with a finite isobaric volume change leads to a coupling between **devolatilization kinetics**, temperature, and fluid pressure, but this coupling does not hinder the evolution of porosity waves (Connolly 1997). Finite volume change reactions also influence the initial pressure distribution, but regardless of this distribution, deformation will cause the system to evolve toward a state in which effective pressures are low or negative at the top of the reacted region. For example, a reaction with a positive (isobaric) volume change may initially generate fluid overpressure throughout the reacted rocks, with the result that hydraulic diffusion drives fluid both upward and downward from the reaction front. Thus the flux within the reacted rocks is not constrained by symmetry. However, provided the permeability within the reacted rocks is much higher than in the surroundings, the fluid pressure gradient will approach the hydrostatic value. Thus, the greatest overpressures will occur at the top of the reacted column. This distribution must lead to higher rates of dilational deformation at the top of the column and, ultimately, underpressured porosity at depth.

Despite the complexities that may influence the kinetics of individual devolatilization reactions, there is reason to believe that overall rates of metamorphic devolatilization do not differ greatly from those predicted by equilibrium models. Specifically, if rocks cannot sustain large fluid overpressures then the thermal overstepping of the equilibrium conditions is likely to be the primary manifestation of disequilibrium. As reaction kinetics are often an exponential function of

851 temperature (Rubie and Thompson 1985), moderate thermal overstepping should  
852 accelerate kinetics to the point at which they become limited by the rate of energy  
853 input as would be the case for an equilibrium system. This logic assumes that rocks  
854 cannot support large elastic stresses. That this assumption is not a universal truth  
855 has been demonstrated in experiments on reactive systems in which a fluid inclu-  
856 sion achieves a non-hydrostatic equilibrium with its surroundings (Kerschhofer  
857 et al. 1998; Mosenfelder et al. 2000; Milke et al. 2009). Vrijmoed et al. (Vrijmoed  
858 et al. 2009) argue that strength contrasts in rocks are capable of generating large  
859 scale fluid inclusions that sustain pressures far above the lithostatic load. An effect  
860 of this nature has been invoked to explain the seemingly metastable persistence of  
861 volatile-bearing rocks (Padron-Navarta et al. 2011).

#### 862 **14.5.4 Multidimensional Viscous Porosity Waves**

863 The 3-d expression of the 1-d porosity wave just discussed corresponds to a sill-like  
864 structure (Fig. 14.9b). However in two and three dimensions both numerical (Scott  
865 and Stevenson 1986; Stevenson 1989; Wiggins and Spiegelman 1995) and analyti-  
866 cal (Barclon and Lovera 1989) models show that 1-d solitary waves are unstable  
867 with respect to circular and spherical solitary waves. This instability is  
868 demonstrated numerically for fluid flow from a high porosity region, an analogy  
869 for a metamorphic fluid source, by introducing random noise into the initial  
870 porosity distribution (Fig. 14.9a). Although the 2-d waves (Fig. 14.9c) appear  
871 significantly different from the 1-d waves (Fig. 14.9b) that evolve from the initial  
872 porosity distribution without noise, it emerges that their properties are well  
873 approximated by applying radial symmetry to the porosity distribution of the 1-d  
874 solitary wave solution (Connolly and Podladchikov 2007). Thus, 1-d and 2-d  
875 solitary waves have an essentially equivalent relation between amplitude and  
876 speed. Although untested, it is assumed that the same approximation can be made  
877 in 3-d by applying spherical symmetry to the 1-d porosity distribution. That the 2-d  
878 approximation is nearly exact in the limit that the maximum porosity is  $> 10 \phi_0$  is  
879 verified by comparing the relationship between wave velocity and amplitude in  
880 analytic (Fig. 14.8) and numerical results (Fig. 14.9). The reason for the increased  
881 speed of 2-d waves compared to 1-d waves emanating from a comparable source is  
882 primarily the effect of a weak spatial focusing of the source flux in the 2-d case. The  
883 most important distinction between planar and circular waves is the existence of  
884 strong lateral pressure gradients associated with the dipolar pressure field of  
885 circular waves (Figs. 14.9d and 14.10a). Thus, in contrast to the unidirectional  
886 fluid flow of planar waves, fluid flow in circular waves is characterized by a circular  
887 pattern in which lateral fluxes are of comparable magnitude (Scott 1988; Connolly  
888 2010). The circular pattern develops in the reference frame of the wave  
889 (Fig. 14.10a), but, in the reference frame of the solid matrix, passage of a wave is  
890 marked first by fluxes with a lateral component away from the vertical axis of the  
891 wave, followed by a period in which the lateral component is directed toward the  
892 axis. During this oscillation, the vertical component of the flux is always upward.

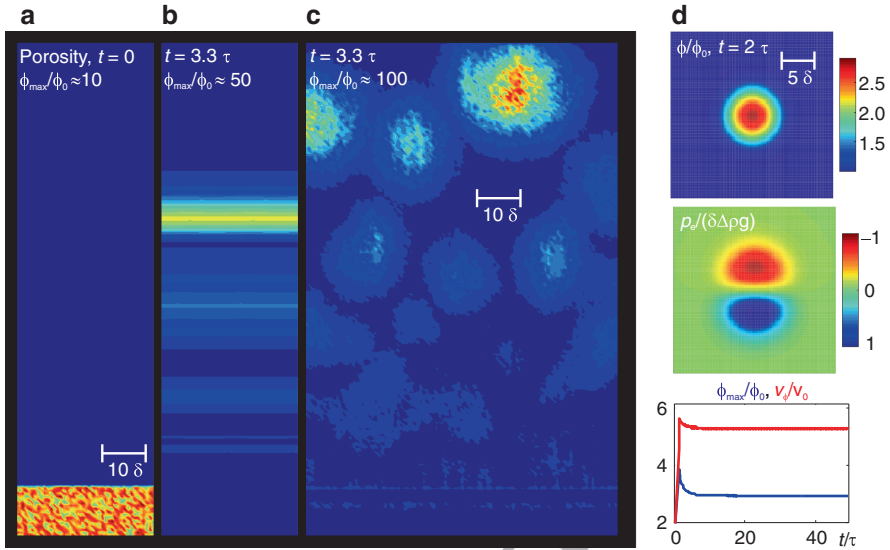


**Fig. 14.9** Two-dimensional numerical simulations of porosity waves initiating from high porosity horizons that differ only in that in one case random noise is added to the initial porosity distribution. The simulations are for a Newtonian matrix ( $n_\sigma = 1$ ,  $n_\phi = 3$ ). If the initial porosity is perfectly smooth, 1-d sill-like waves nucleate from the source (b). However, if white noise is added to the initial porosity distribution as depicted in (a), the 1-d waves become unstable with respect to circular 2-d waves (c). The 2-d waves cause spatial focusing of the source flux. Consequently the 2-d waves have larger amplitudes and higher velocities than 1-d waves initiating from a similar source. Numerical simulations have also shown that the stable viscous solitary wave geometry in 3-d is spherical (Wiggins and Spiegelman 1995). (d) A numerical simulation of a 2-d wave nucleated from a small circular source region, illustrating the dipolar effective pressure field and the short duration of transient effects (i.e., the wave has essentially reached a steady state by  $t/\tau \sim 2$ ). Wave properties along the vertical axis of 2-d waves, with  $\phi_{\max}/\phi_0 > 10$ , are indistinguishable from those predicted for 1-d waves with the same amplitude (Connolly and Podladchikov 2007)

### 14.5.5 Porosity Waves in an Upward Strengthening Crust

893

The preceding discussion has ignored the temperature dependence of the viscous 894 rheology, which is responsible for the upward strengthening of the lower crust. 895 From Eq. 14.12, the compaction length and time scales increase exponentially with 896 decreasing temperature towards the Earth’s surface, increasing by a factor of 897  $(n_\sigma + 1)^{-1}$ , for a decrease in depth comparable to the viscous e-fold length  $l_A$  898 (Eq. 14.15, Fig. 14.1). This effect makes achievement of true steady-state waves 899 a mathematical impossibility because the compaction scales vary between the top 900 and bottom of a wave (Connolly 1997). The strength of this variation can be 901 assessed by comparing the steady-state wavelength  $\lambda$  to  $l_A$ . If  $\lambda \ll l_A$ , then the 902 rheological variation within the wave is weak and a **quasi-steady state** may arise 903 such that at any point in time the properties of the wave closely approximate the 904

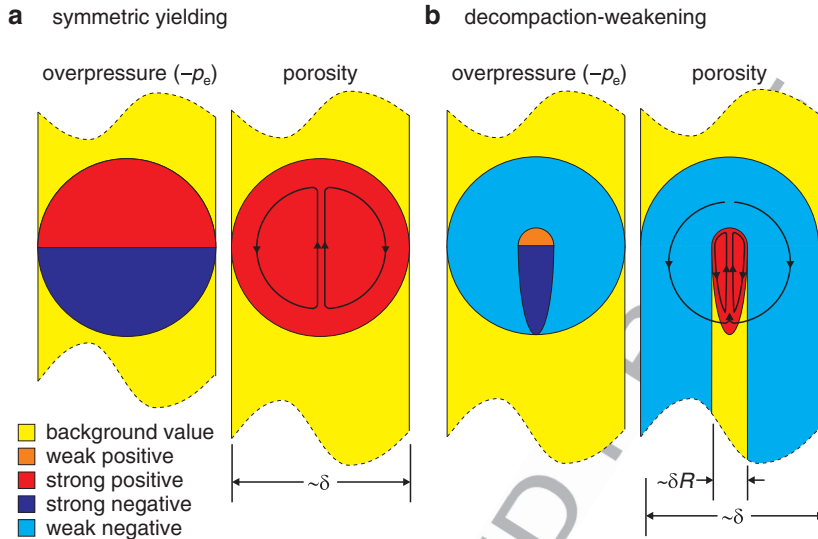


**Fig. 14.10** Illustration of the scaling arguments used to relate the solitary wave solution in the symmetric viscous case (a) to the solitary waves that develop in a matrix with decompaction weakening (b). Colors indicate regions of the matrix that are characterized by weakly and strongly depressed or elevated values of overpressure and porosity. Approximate fluid flow paths, relative to a reference frame that moves with the porosity wave, are shown in the porosity map. The true paths do not close because the wave is subject to a small fluid flux from the background porosity (Fig. 14.7). This discrepancy is insignificant in large amplitude waves. In the reference frame of the solid, the vertical component of compaction driven fluxes is upward. In the symmetric case, the pressure distribution associated with a porosity wave is an antisymmetric dipole that induces balanced fluid circulation so the wave has no tendency to gain or lose mass (Fig. 14.11d). With decompaction weakening, fluid underpressures and compaction develop on the length scale  $\delta$  as in the symmetric viscous case, whereas decompaction and overpressure develop on the shorter length scale  $\delta R$ . Thus, decompaction generates an elevated region of porosity and pressure analogous to the upper hemisphere of the symmetric viscous case, but on this shorter length scale. Restoration of this elevated porosity occurs on the length scale  $\delta$ , which causes the compacting portion of the wave to develop a semi-ellipsoidal geometry. Fluid underpressure in the compacting region relaxes on the length scale  $\delta$  causing compaction of the matrix in advance of the wave as well as in laterally adjacent portions of the matrix that have not been perturbed by decompaction. The asymmetric pressure distribution causes unbalanced fluid circulation, with the result that the wave gains mass from the matrix as it propagates, this imbalance is indicated schematically by the outermost, unclosed, flow path

905 steady state. In this regime, waves will slow and spread as they propagate upward.  
 906 In the limit  $\lambda \rightarrow l_A$  this quasi-steady state becomes infeasible because compaction  
 907 within a wave occurs much more rapidly than decompaction. At this point, the local  
 908 compaction length scale becomes meaningless for compaction processes in the  
 909 vertical direction, and  $l_A$  determines the vertical length scale (Connolly and  
 910 Podladchikov 1998). In the absence of strong lateral thermal gradients, as assumed  
 911 here, the local compaction length dictates the scale of lateral processes, thus,

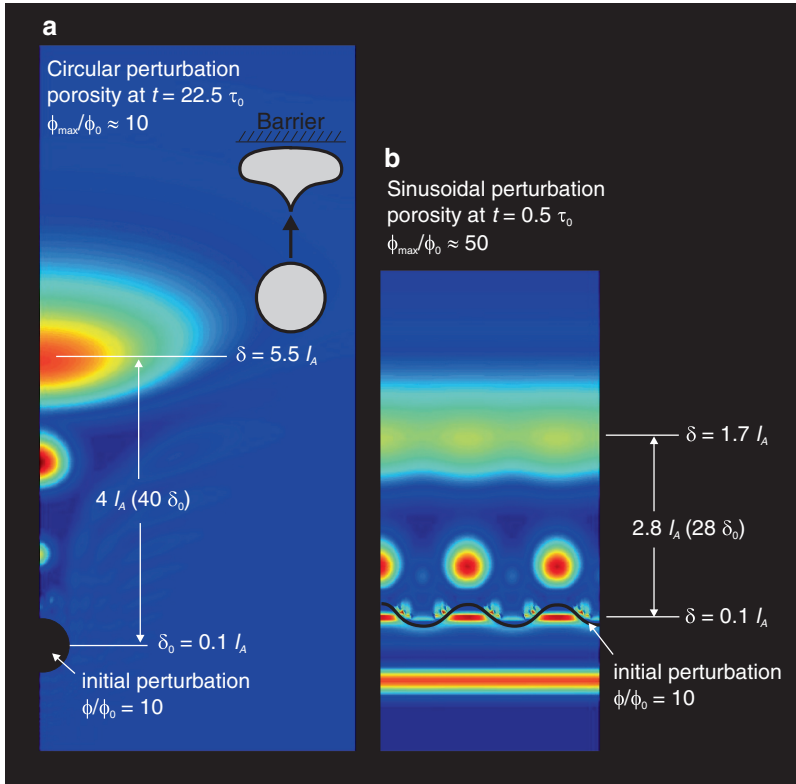


**Fig. 14.11** Two-dimensional numerical simulations of viscous porosity waves in a rock matrix that strengthens upward due to thermal activation on the length scale  $l_A$  (Fig. 14.1). This effect causes the local compaction length  $\delta$  to increase upward from its initial value  $\delta_0$ ; the simulations are for Newtonian rheology ( $n_\sigma = n_\phi = 3$ ). **(a)** If the source is at depth such that  $\delta_0 < l_A$ , the quasi-steady state waves mimic the circular viscous steady-state, but spread as they rise upward until their wavelength approaches  $l_A$  at which point the waves flatten to oblate ellipsoids with vertical length scale  $l_A$  and horizontal length scale  $\delta$ . The wave velocities decay exponentially upward on the length scale  $l_A$ . **(b)** Waves are generated from a high porosity layer with a sinusoidal upper boundary at depth such that  $\delta_0 < l_A$ . This simulation demonstrates that the effect of thermal activation is to restabilize 1-d solitary waves when wavelength approaches  $l_A$  (Modified from Connolly and Podladchikov (1998))

thermal activation gives rise to an intrinsic anisotropy to compaction-driven fluid flow. 912 913

The consequences of thermal activation for the 2- and 3-d viscous solitary wave solutions is demonstrated by a numerical experiment in which upward propagating waves are induced from a circular source (Fig. 14.11a). At the initial depth, the waves are small in comparison to  $l_A$  and approximate the circular 2-d steady state. As the waves migrate upward their wavelength becomes comparable to  $l_A$  and they flatten to ellipsoidal structures with the horizontal length scale controlled by the local value of  $\delta$  and the vertical length scale limited by  $l_A$ . A second numerical 914 915 916 917 918 919 920

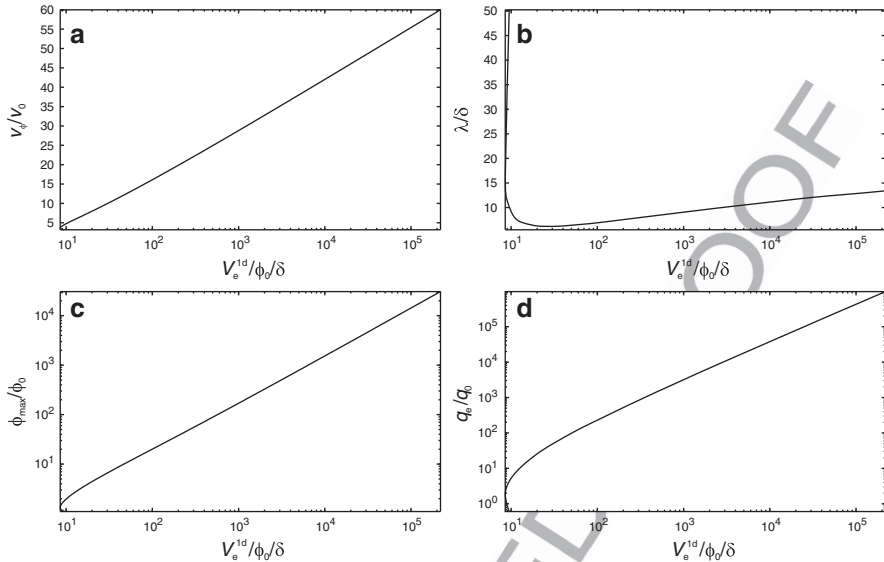


**Fig. 14.12** Steady-state 1-d solitary wave properties in a power law ( $n_\sigma = n_\phi = 3$ ) viscous matrix as a function of the excess volume ( $V_e^{1d}$ , Eq. 14.26). These properties can be used to predict quasi-steady state wave evolution in upward strengthening rocks as a function of the local compaction length. See text for discussion

921 experiment, in which waves initiating from a horizontal source are destabilized by a  
 922 perturbation, shows that the effect of thermal activation is to restabilize 1-d planar  
 923 waves (Fig. 14.11b). To show that this process is relevant to crustal fluid flow it is  
 924 necessary to show that the wavelength of quasi-steady state waves will approach the  
 925  $l_A$  at the brittle-ductile transition (Fig. 14.1). This cannot be established from wave  
 926 properties expressed as a function of excess flux because this flux decays as waves  
 927 slow. However, quasi-steady state waves may conserve the excess fluid volume

$$V_e = \iiint (\phi - \phi_0) dx dy dz \quad (14.27)$$

928 and therefore wave evolution can be predicted as a function of  $V_e$  (Fig. 14.12)  
 929 provided  $\lambda < l_A$ . There are two complications in such predictions. The more  
 930 difficult is that if waves evolve from 3-d structures, it is necessary to account for  
 931 lateral variations in porosity. To avoid this complexity, the waves are approximated  
 932 here as 1-dimensional. This approximation has the consequence that waves  
 933 lengthen more rapidly than they would if 3-d geometry were taken into consider-  
 934 ation. The second complication is that the dimensionless excess volume has  
 935 a minimum at  $V_e^{1d}/\delta/\phi_0 \sim 8$  (Fig 14.13a), thus a wave that initiates with  
 936  $V_e^{1d}/\delta/\phi_0 > 8$  and broadens upward due to thermal activation cannot increase its  
 937 wavelength above  $\lambda_{max} \sim 17 \delta$ , the wavelength at  $V_e^{1d}/\delta/\phi_0 \sim 8$ , and must decay to  
 938 the dissipative periodic solution as it propagates above this point, i.e., at  $v_\phi \approx 3.5$   
 939  $v_0$ , slightly above the minimum velocity at which the solitary solution is stable.

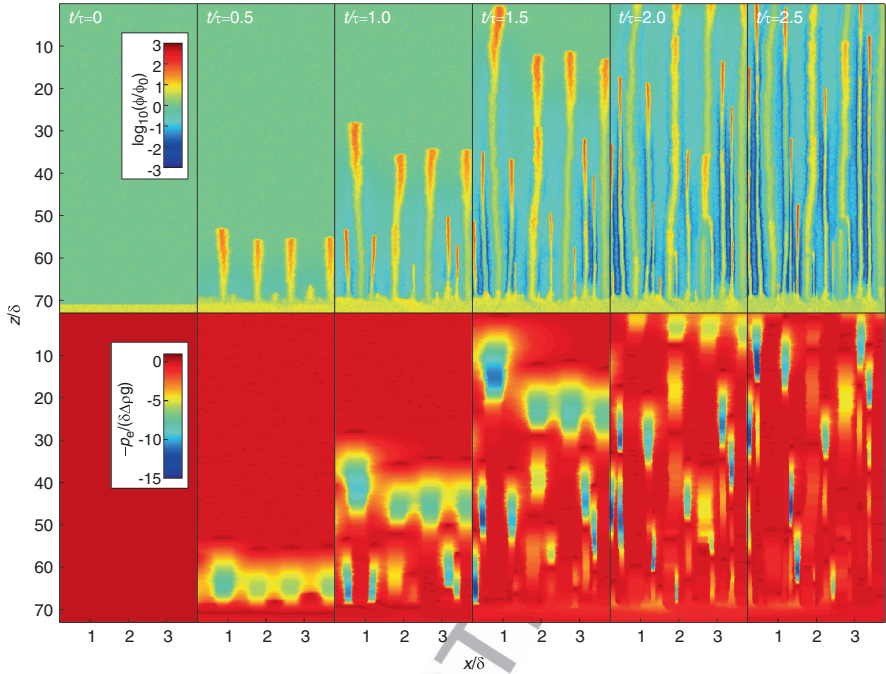


**Fig. 14.13** Two-dimensional numerical simulation of fluid flow through a matrix with decompaction weakening ( $R = 0.03$ ) as it evolves from a layer with elevated porosity of thickness  $60 \delta$  that is bounded from above and below by regions with an order of magnitude lower porosity. *Upper panels* show porosity in the uppermost portion of the layer and in the overlying region. *Lower panels* show the corresponding distribution of fluid overpressure. Initial waves ( $t = \tau/2$ ) form with characteristic spacing identical to the viscous compaction length and leave a trail of slightly elevated porosity, flanked by a fluid depleted matrix. Depletion of the matrix reduces the local compaction length scale for the initiation of subsequent waves ( $t = \tau$ ). These waves collect within the trails of the initial waves, so that at  $30\text{--}40 \delta$  from the initial obstruction, flow is again channelized on the length scale  $\delta$ . By analogy with the 3-d viscous case (Wiggins and Spiegelman 1995), it is presumed that the 3-d expression of the channels would be pipe-like structures. However, in the presence of far field stress, kinematic effects would flatten the tubes in the direction of the minimum horizontal stress (Modified from Connolly and Podladchikov (2007))

Returning to the amphibolite-facies example (Sect. 14.5.2), if thermal activation is the sole source of variability in the compaction scales, then from Eqs. 14.12, 14.23, and, 14.24, as a function of temperature the compaction scales can be expressed as

$$\delta = \delta_0 \exp \left[ \frac{Q}{n_\sigma + 1} \frac{T_0 - T}{TT_0} \right] \tag{14.28}$$

and

$$\tau = \tau_0 \exp \left[ \frac{Q}{n_\sigma + 1} \frac{T_0 - T}{TT_0} \right], \tag{14.29}$$

944 where  $T_0$  is the temperature at which the scales are  $\delta_0$  and  $\tau_0$ . For  $Q = 250$  kJ/mol,  
 945  $n_\sigma = 3$ ,  $\delta_0 = 31$  m, and  $\tau_0 = 10$  ky, and estimating the temperature of the amphib-  
 946 olite facies metamorphism as  $T_0 = 848$  K; ~~then~~ the initial length and time scales  
 947 increase to 780 m and 250 ky at the temperature of the brittle-ductile transition  
 948 ( $\sim 623$  K). For  $q_e/q_0 = \bar{q}/q_0 = 10^2$ , from the initial wave speed  $v_\phi/v_0 = 12.2$   
 949 (Fig. 14.8a),  $V_e^{1d}/\delta_0/\phi_0 = 49$  (Fig. 14.12a) and, if  $V_e^{1d}$  and  $\phi_0$  are constant, then at  
 950 the brittle-ductile transition, ~~the~~  $V_e^{1d}/\delta_1/\phi_0 = (V_e^{1d}/\delta_0/\phi_0)(\delta_0/\delta_1) = 2.0$ . This  
 951 value is below the minimum in  $V_e^{1d}/\delta/\phi_0$ , so in this case the wave would reach  
 952  $\lambda_{\max}$  below the brittle-ductile transition, at which point it would begin to evolve  
 953 toward the periodic wave solution. For the case  $q_e/q_0 = \bar{q}/q_0 = 10^4$ , the initial wave  
 954 has  $v_\phi/v_0 = 36$  and  $V_e^{1d}/\delta_0/\phi_0 = 3400$ , so at the brittle-ductile transition  
 955  $V_e^{1d}/\delta_1/\phi_0 = 140$ . From this value of  $V_e^{1d}/\delta/\phi_0$  (Fig. 14.12), the quasi-steady  
 956 state wave has  $v_\phi/v_0 = 18$ ,  $\lambda/\delta_1 = 7.2$ ,  $\phi_{\max}/\phi_0 = 28$ , and  $q_e/q_0 = 67$ . As this  
 957 wavelength (5,600 m) exceeds  $l_A$  it may be concluded that the flow processes  
 958 would cease to be controlled by the viscous steady-state at greater depth. For this  
 959 particular case, the overpressure associated with the wave ( $\sim 50$  MPa) near the  
 960 brittle-ductile transition might be sufficient to provoke a change from viscous to  
 961 plastic dilational deformation. In the absence of such a change, viscous waves are  
 962 expected to die at depth, with smaller waves dying at greater depth. Death, in this  
 963 context, means simply that the behavior of the system cannot be predicted in terms  
 964 of the steady state. What can be predicted is that in its death throes a viscous wave  
 965 will produce a sub-horizontal fluid-rich domain, with thickness comparable to  $l_A$   
 966 beneath the brittle-ductile transition.

### 967 14.5.6 Hydrofracture and Decompaction-Weakening

968 The viscous porosity wave mechanism requires overpressures of the same magni-  
 969 tude as the effective pressures that cause compaction ( $\sim \lambda \Delta \rho g/2$ ). If these  
 970 overpressures are greater than rock tensile strength, they induce plastic dilational  
 971 strain by macroscopic or microscopic **hydrofracturing**, the latter manifestation  
 972 being favored at high temperature (Hill 1950). Returning to the schematic devolati-  
 973 lization scenario considered in the viscous case (Fig. 14.6a), the greatest  
 974 overpressures must occur at the top of the reacted horizon, thus repeated  
 975 hydrofracturing will propagate porosity into the overlying rocks. Provided the  
 976 hydrofracturing occurs on a length scale that is small in comparison to the viscous  
 977 compaction length  $\delta$ , the rate of propagation is limited by the rate at which  
 978 compaction at depth supplies fluid to the hydrofracture front. Thus, in 1-d there is  
 979 a steady state in which fluid driven upward through a porous domain, by viscous  
 980 compaction at depth, is accommodated by hydrofracturing at overpressures that are  
 981 much smaller than the effective pressures required for compaction (Fig. 14.6c). The  
 982 difficulty in quantifying this steady-state is that it is dependent on details of the  
 983 hydrofracture mechanism (Rozhko et al. 2007). An approximation that circumvents

this complexity is to assume that the effect of plasticity is to reduce the effective 984  
viscosity of rocks undergoing decompaction. The assumption is justified if 985  
hydrofracture and viscous dilation occur in tandem, because the effective behavior 986  
is then viscous; but characterizing this behavior by a single parameter is ad-hoc. For 987  
present purposes, the parameter chosen to characterize a relative weakening in 988  
decompaction is 989

$$R = \sqrt[n_{\sigma}+1]{A/A_d}$$

where  $A_d$  is the coefficient of viscous flow during decompaction, i.e.,  $R < 1$ . The 990  
reason for using  $R$  rather than  $A_d$  to characterize **decompaction-weakening** is that  $R$  991  
is the proportionality constant that relates the length scales for decompaction and 992  
compaction, i.e., the decompaction length is  $\delta_d = R\delta$ . If decompaction weakening 993  
maintains fluid overpressures near the tensile strength  $\sigma_y$ , then  $R$  is related to  $\sigma_y$  by 994

no new paragraph

$$\sigma_y = \delta_d \Delta \rho g = R \delta \Delta \rho g. \quad (14.30)$$

Equation 14.30 results in a parameterization that is consistent with the expecta- 995  
tion that overpressure is limited by the rock tensile strength, but it does not justify 996  
the formulation. 997

In the 1-d case, the existence of a solitary wave solution for a matrix with 998  
decompaction-weakening requires only that it is possible to connect the viscous 999  
solitary wave solution for the decompacting region, with length scale  $R\delta$ , with the 1000  
viscous solution for the compacting region, with length scale  $\delta$ . Because the 1001  
relationship between wave velocity and amplitude is independent of the coefficient 1002  
of viscous flow (Eq. 14.55, Appendix), this connection is possible in 1-d and 1003  
identical to the viscous solitary wave solution except that the overpressured portion 1004  
of the wave scales as  $R\delta$  rather than  $\delta$ . Compaction is the rate limiting process for 1005  
the combined solution, with the result that the time scale for the steady state is 1006  
unchanged from the viscous case. Moreover, for strong manifestations of plasticity, 1007  
i.e.,  $R \ll 1$ , the extent of the overpressured portion of the wave is insignificant, 1008  
with the result that the wave solution for decompaction-weakening is well 1009  
approximated by the lower half of the viscous solution. In numerical simulations, 1010  
such waves appear as self-propagating fluid compartments within which fluid 1011  
pressure rises along a hydrostatic gradient to pressures slightly above the lithostat 1012  
(Connolly and Podladchikov 2000). 1013

Decompaction-weakening results in a rheology in which rocks weaken in the 1014  
direction of compaction-driven flow. This effect is the opposite of thermal activa- 1015  
tion in the viscous case, which leads to flattening of porosity waves (Fig. 14.11). 1016  
Thus, decompaction-weakening causes waves to elongate in the direction of flow 1017  
inducing channelization (Fig. 14.13). The channels are generated by tube-like 1018  
porosity waves of extraordinary amplitude and speed that leave a trail of incom- 1019  
pletely compacted porosity in their wake. These trails act as preferential pathways 1020  
for subsequent fluid flow, and develop initially with spacing  $\sim \delta$  and width  $\sim R\delta$ , a 1021

1022 geometry that amplifies the source fluid flux by a factor of  $\sim 4/R^2$ . This pattern of  
 1023 fluid flow corresponds to that inferred in greenschist-facies rocks by Skelton et al  
 1024 (2000), who propose that the flow was episodic and propagated by microcracking.  
 1025 Similar flow patterns have also been inferred in asthenospheric systems (Jagoutz  
 1026 et al. 2006; Bouilhol et al. 2009; Bouilhol et al. 2011).

1027 The tube-like waves are propagated by a region of overpressure that decompacts  
 1028 the matrix (Fig. 14.13). A much larger region of underpressure, beneath the  
 1029 overpressured region, is necessary for compaction to expel fluid at the rate required  
 1030 to fill the porosity created by decompaction. ~~As compaction occurs, on the scale  $\delta$~~   
 1031 ~~and decompaction on the scale  $R\delta$ , the asymmetric pressure distribution induces~~  
 1032 ~~unbalanced fluid circulation (Fig. 14.10b). This imbalance causes the waves to gain~~  
 1033 ~~fluid by draining the porosity in the surrounding matrix. The gain in fluid obviates a~~  
 1034 ~~steady state, but the speed-amplitude relation of the waves is essentially identical to~~  
 1035 ~~the symmetric viscous case suggesting a quasi-steady state. This quasi-steady state~~  
 1036 ~~can be explained by observing that if decompaction is much more rapid than~~  
 1037 ~~compaction, then the decompacting region will develop with the characteristics of~~  
 1038 ~~the upper hemisphere of the 2- or 3-d viscous solution on the length scale  $R\delta$ .~~  
 1039 ~~Compaction restores the porosity generated by decompaction on the length scale  $\delta$ ,~~  
 1040 ~~thus the compacting region will approximate the lower half of a prolate ellipsoid~~  
 1041 ~~(Fig. 14.10b). The associated fluid volume is  $R^2V_c^0/2$ , where  $V_c^0$  is the fluid volume~~  
 1042 ~~of the 3-d spherical viscous solution (Eq. 14.27), which is approximated by~~  
 1043 ~~applying spherical symmetry to the porosity distribution of the 1-d viscous solution.~~  
 1044 ~~For  $R$  in the range  $10^{1/2}$ – $10^3$  this model has been verified by comparison with~~  
 1045 ~~numerical simulations for linear viscous rheology ( $n_\sigma = 1$ , Connolly and~~  
 1046 ~~Podladchikov 2007). These simulations also show that, in the absence of thermal~~  
 1047 ~~effects, wave amplitude grows as~~

$$\partial\phi_{\max}/\partial t \approx \phi_0 / (\tau R^{3/4}). \quad (14.31)$$

1048 and that the speed-amplitude relation of waves is essentially identical to the steady  
 1049 solitary wave solution in a viscous matrix without decompaction-weakening if the  
 1050 simple viscous matrix is characterized by the  $AR^{n_\sigma+1}$ . This latter result implies that  
 1051 the effective time-scale for compaction-driven fluid flow in a decompaction-  
 1052 weakening matrix is dictated by the viscous response of the weak, overpressured,  
 1053 rocks, i.e., the effective time-scale is

$$\tau_d \approx \tau R. \quad (14.32)$$

no new paragraph

1054 Given the ad-hoc nature of the parameterization further quantification is unwar-  
 1055 ranted, but the role of plastic yielding should increase with falling temperature  
 1056 because  $\delta$  is strongly dependent on temperature, but yield strength is weakly  
 1057 temperature dependent. Thus, a decompaction-weakening rheology causes  
 1058 compaction-driven fluid flow to become increasingly focused towards the surface,  
 1059 the antithesis of the behavior of the symmetric viscous case.

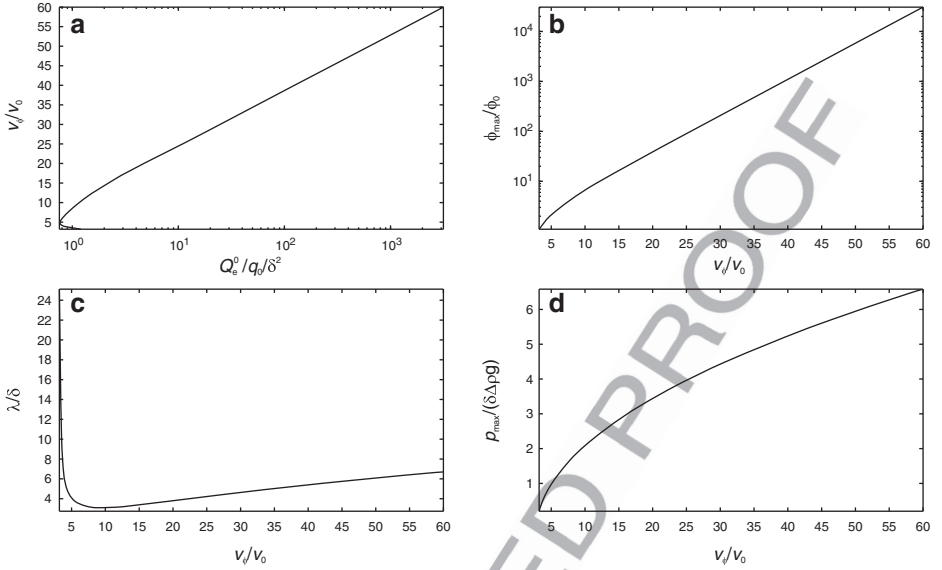


**Fig. 14.14** Quasi-steady state solitary wave properties (for  $n_\sigma = n_\phi = 3$ ) for a decompaction-weakening viscous rheology as a function of  $Q_e^0$ . For  $R \ll 1$ , the volumetric rate of fluid transport by a wave is  $Q_e \approx Q_e^0 R^2$ . Equating this rate to the source flux that is focused into the wave,  $Q_s \approx 4\bar{q}\delta^2$ , yields the value of  $Q_e^0/\delta^2 q_0$  (i.e.,  $4\bar{q}/R^2 q_0$ ). This value is appropriate to predict the properties of the 3-d tube-like waves that would nucleate from a dehydrating horizon

Decompaction weakening causes fluid flow within a horizontal source region to be focused into tube-like channels of width  $R\delta$  with a characteristic spacing  $\delta$ . The properties of the waves responsible for channel formation can be predicted as a function of  $R$  and fluid production within the source region if, as before, a balance between fluid transport and production is assumed. The symmetry of the quasi-steady state is such that for  $R \ll 1$  the rate of fluid transport, by a wave, is  $Q_e \approx Q_e^0 R^2$ , where  $Q_e^0 = V_e^0 v_\phi / \lambda / 2$  is half the rate for the viscous rheology ( $R = 1$ ). Approximating the area drained by a channel as a square of area  $4\delta^2$ , the vertically-integrated fluid production rate within the source region is  $Q_s \approx 4\bar{q}\delta^2$ . Equating  $Q_e$  and  $Q_s$ , rearranging the result, and dividing through by  $q_0$  to make the result non-dimensional, yields

no new paragraph

$$\frac{Q_e^0}{\delta^2 q_0} \approx \frac{4\bar{q}}{R^2 q_0}. \tag{14.33}$$

Given  $Q_e^0$  from Eq. 14.33, wave speed, amplitude, and wavelength, which are independent of  $R$ , are recovered from the properties of the steady-state (Fig. 14.14). In the absence of experimental or theoretical constraints, field evidence of channelized fluid flow can be used to infer the  $R$  values necessary to explain

1075 channelization by decompaction weakening. Channelization patterns are difficult to  
 1076 discern at low metamorphic grades, but at higher temperatures patterns associated  
 1077 incipient charnockitization (Stahle et al. 1987) and pervasive melt migration  
 1078 (Jagoutz et al. 2006; Bouilhol et al. 2009; Bouilhol et al. 2011) are broadly  
 1079 consistent with  $R \sim O(10^{-1})$ . Adopting this value for the scales of the amphibolite  
 1080 facies example considered previously ( $\delta = 31$  m and  $\tau = 10$  ky), a miniscule  
 1081 flux perturbation of  $\bar{q}/q_0 = 2$  ( $Q_c^0/\delta^2/q_0 = 800$ ) is adequate to generate a wave  
 1082 that travels with speed  $v_\phi = 51 \delta/\tau = 160$  m/ky, vertical dimension  $\lambda = 6\delta = 190$   
 1083 m, horizontal dimension  $R\lambda = 19$  m,  $\phi_{\max} = 0.7$ ,  $p_{\max} = 4$  MPa ( $\sim\lambda\Delta\rho g$ ), and  
 1084  $p_{\min} = -0.4$  MPa ( $\sim R\lambda\Delta\rho g$ ). Although the amplitude of this wave violates the  
 1085 small-porosity approximation used to derive the steady-state properties, it  
 1086 demonstrates the extraordinary efficacy of 3-d focusing. In nature, such instabilities  
 1087 would be likely to provoke an alternative transport mechanism such as fracture-  
 1088 controlled flow.

## 1089 14.6 Adding Details

1090 The suggestion that lower crustal fluid flow is accomplished by the propagation of  
 1091 fluid-rich domains that correspond to some esoteric solution of the compaction  
 1092 equations cries for evidence and provokes the suspicion in the minds of field-based  
 1093 geologists that they are being sold a geological analog to the proverbial spherical  
 1094 cow of theoretical physics. The model is the mathematical consequence of a set of  
 1095 essential assumptions that are, at least individually, accepted in geoscience; the  
 1096 purpose of this Chapter is to draw attention to this consequence rather than to prove  
 1097 that it corresponds to reality. If there is a spherical cow to be found, then it must be  
 1098 lurking among these assumptions. The assumptions are: (1) that when a fluid is  
 1099 present its pressure is near lithostatic; (2) that flow is governed by Darcy's law; (3)  
 1100 that permeability is continuous and a strong function of connected porosity; and (4)  
 1101 that compaction occurs by a viscous mechanism (e.g., dislocation or pressure-  
 1102 solution creep) in response to effective pressure. In rejecting the model, it behooves  
 1103 the skeptic to decide which of these assumptions is false. The fourth assumption is  
 1104 treacherous at small porosities because omnipresent elastic mechanisms may limit  
 1105 viscous response (Connolly and Podladchikov 1998; Bercovici et al. 2001). How-  
 1106 ever, if these assumptions are accepted, the consequence is that fluid flow must be  
 1107 episodic and accompanied by oscillations in fluid pressure, even in an idealized  
 1108 homogeneous crust perturbed by an idealized devolatilization reaction. As a pre-  
 1109 diction, this result is mundane because there is no geologic evidence to the contrary;  
 1110 its value is only that it offers a consistent explanation for such phenomena that, in  
 1111 principle, can be tested against observation. The purpose of modeling is not to  
 1112 emulate the complexity of nature, rather to explain it. For this reason, the models  
 1113 presented here sacrifice detail, but it is undeniable that the details of natural systems  
 1114 will influence fluid flow. A comprehensive discussion of this influence is

impractical; however, it is appropriate to consider some circumstances when the effect of such details can be neglected or anticipated.

### 14.6.1 Large-Scale Lateral Fluid Flow

Metamorphic devolatilization reactions have the capacity to produce high porosity layers, within which the compaction length,  $\delta_1$ , may be orders of magnitude greater than it is in the surrounding rocks. In principle such a layer has the capacity to conduct lateral fluxes on the length scale  $\delta_1$ ; however, in the absence of external forcing, the pressure gradients responsible for lateral fluxes are limited by the spacing of the porosity waves that effect drainage through the low porosity surroundings. This spacing is dictated by the compaction length in the unperturbed matrix, which therefore determines the length scale for lateral fluid flow (Figs. 14.9 and 14.13). Therefore, it seems probable that large-scale lateral fluid flow inferred from metamorphic field studies (e.g., Ferry and Gerdes 1998; Skelton 1996; Wing and Ferry 2007) is induced by external perturbations, such as drainage caused by tectonically-induced dilatant shear zones (Sibson 1992) or mean stress variations caused by folding (Schmalholz and Podladchikov 1999; Mancktelow 2008). The strength of these perturbations increases rock strength, thus they are likely to become important under the same conditions that embrittlement may cause a decompaction-weakening rheology (Sect. 14.5.6). Because decompaction weakening reduces the time-scale for dynamic drainage by porosity waves through the unperturbed matrix, the influence of an externally imposed drain will be dependent on the relative magnitudes of the time scale for within-layer flow

$$\tau_1 = \tau_0 \left( \frac{\phi_0}{\phi_1} \right)^{\frac{n_\sigma (n_\phi - 1)}{n_\sigma + 1}} \quad (14.34)$$

and the effective time scale  $\tau_{dw}$  (Eq. 14.32) for dynamic drainage by decompaction weakening, such that the process that operates on the shorter time-scale will dominate (Fig. 14.15). For the case  $\tau_1 = \tau_d$ , numerical simulation of fluid flow caused by the intersection of a permeable fracture zone with a metamorphic reaction front (Fig. 14.5 of Connolly 2010) shows that lateral flow occurs toward the fracture zone on the length scale  $\delta_1$  for  $t < \tau_d$ , but occurs only on the shorter length scale  $\delta_0$ , and is independent of the fracture zone, at  $t > \tau_d$ . It is of course possible that a reaction generates a highly permeable layer that is sealed from above by a different, impermeable, lithology. In this case, the lateral flow can occur on the length scale  $\delta_1$ . As evidence for large-scale lateral flow appears to come primarily from low and moderate grade metamorphic rocks, a more probable explanation for the phenomenon is that the flow occurs at conditions such that  $\delta < l_A$ . Under such conditions (Fig. 14.11), the vertical scale for compaction driven flow is  $l_A$ , but the horizontal length scale is the local value of  $\delta$ , which increases exponentially with falling temperature.

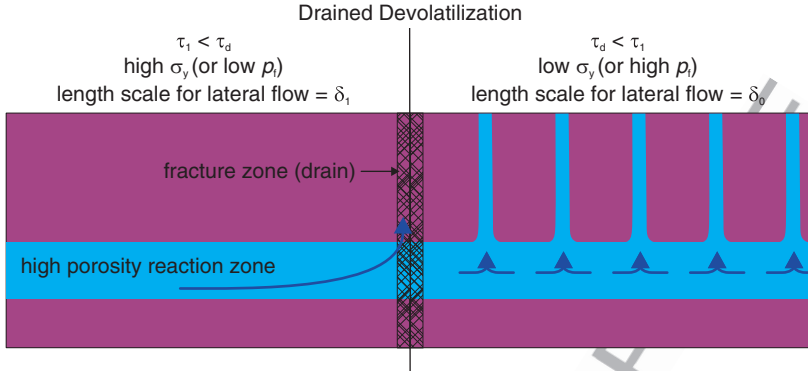


**Fig. 14.15** Schematic of the influence of a drain (e.g., a permeable fracture zone) on fluid flow within a high porosity horizon generated by a devolatilization reaction. If the compaction time and length scales in the unperturbed matrix are  $\tau_0$  and  $\delta_0$ , and the porosity in the horizon is  $\phi_1$ , then the corresponding scales within the horizon are, for  $n_\sigma = n_\phi = 3$ ,  $\delta_1 = (\phi_1/\phi_0)^{1/2}\delta_0 > \delta_0$  and  $\tau_1 = (\phi_0/\phi_1)^{5/2}\tau_0 < \tau_0$ . Thus, in the absence of decompaction weakening, the drain will draw fluid from the layer on the length scale  $\delta_1$  (as depicted to the left of the drain) because the time scale ( $\tau_1$ ) for within layer flow is shorter than the time scale ( $\tau_0$ ) for the development of dynamic drainage within the unreacted matrix in response to high fluid pressure. If tensile yield strength is  $< \delta_0\Delta\rho g$ , then decompaction weakening reduces the time scale for the development of dynamic drainage to  $\tau_d = \sigma_y/(\delta_0\Delta\rho g)\tau_0$ . Thus, decompaction weakening may lead to circumstances (i.e.,  $\tau_d < \tau_1$ ) in which dynamic drainage dominates and the length scale for lateral fluid within the layer is limited by the compaction length ( $\delta_0$ ) in the unreacted rocks

## 1152 14.6.2 Lithological Heterogeneity

1153 There are two limiting cases for lithological heterogeneity. The trivial case is that  
 1154 the heterogeneity occurs on a scale  $\gg \delta$ . In this case (Fig. 14.16a), the time and  
 1155 length scales relevant for each lithology individually dictate compaction phenom-  
 1156 ena. The alternative is that the heterogeneities are small, relative to the compaction  
 1157 length, in any of the individual lithologies. To illustrate this case (Fig. 14.16b),  
 1158 suppose a vertical sequence of two alternating lithologies in which the layering is  
 1159 thin compared to the compaction length in either layer and that the compaction  
 1160 length in one layer is so much larger than in the other layer that is effectively infinite  
 1161 (i.e., the lithology is rigid). If a porosity wave impinges on such a sequence, the  
 1162 fluid pressure gradient within the rigid layer must rise to supra-lithostatic values to  
 1163 conduct the excess flux carried by the wave, but within the soft layers dilation will  
 1164 cause the fluid pressure gradient to relax to near hydrostatic values. The result is to  
 1165 create a stepped fluid pressure profile that maintains a balance between compaction  
 1166 and dilation on the compaction time and length scales of the soft lithology. An  
 1167 implication of this logic is that the effective rheology for compaction processes in  
 1168 the lower crust is dictated by the rheology of the weakest lithology. In contrast,  
 1169 crustal strength in response to tectonically imposed deformation may be controlled  
 1170 by the strongest lithology, i.e., in the case of homogeneous thickening or thinning.

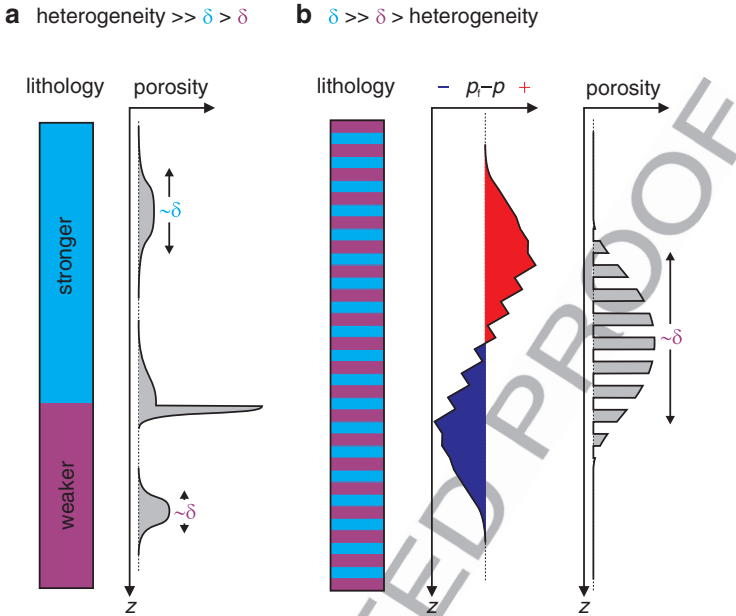


**Fig. 14.16** Schematic of the influence of lithological layering on the propagation of a solitary porosity wave through a viscous matrix. If the layers are thick, compared to the compaction length, within each layer (a), the wave adopts its shape and speed according to the local compaction time and length scales. If the layers are thin compared to the compaction length in either lithology, but the compaction length is much greater in one lithology than it is in the other (b), then the properties of the wave are limited by the compaction scales in the weaker lithology. The effective pressure profile is drawn so that the fluid pressure gradient in the large porosity weak layers is near hydrostatic, and that fluid pressure gradient necessary to conduct the excess flux within the intervening rigid layers is supralithostatic and constant. In reality, because the excess flux varies locally within a solitary wave, the supralithostatic gradients in the rigid layer would decrease toward the tails of the wave.

### 14.6.3 Non-Lithostatic Stress

1171

Compaction-driven flow responds to tectonic stress through its dependence on the mean stress gradient (Eq. 14.5), but local deformation and/or lithological heterogeneity may give rise to strong variations in the far-field stress (Schmalholz and Podladchikov 1999; Mancktelow 2008). As in the case of lithological heterogeneity in a lithostatic crust, the influence of these variations depends upon whether they occur on a spatial scale that is large or small compared to the compaction length scale. Small scale variations will affect local flow patterns, but will not influence the overall tendency of compaction to drive fluid toward low mean stress (strictly in the direction of  $\rho_f g \mathbf{u}_z - \nabla \bar{\sigma}$ , which is vertical in the lithostatic limit). These variations may distort the geometry of the porosity waves that develop in the non-lithostatic case. But because the effective pressure necessary for compaction can only be

1172  
1173  
1174  
1175  
1176  
1177  
1178  
1179  
1180  
1181  
1182

1183 achieved by having hydraulic connectivity on the compaction length scale, the  
1184 distortions are likely to be primarily kinematic.

1185 Large scale **tectonic perturbations** to the lithostatic mean stress gradient can, in  
1186 general, be expected to have relatively minor influence on the rate and direction of  
1187 compaction-driven fluid flow. The greatest influence on rate is realized during  
1188 extension. In such a setting, the relaxation of differential stress in the brittle crust,  
1189 which may be comparable to half the vertical load (Ranalli 1995), will relax over an  
1190  $O(l_A)$  vertical interval (Connolly and Podladchikov 2004), potentially increasing  
1191 the mean stress gradient responsible for, and accelerating, compaction-driven fluid  
1192 flow. Perhaps more importantly, this effect will be amplified within, and favor the  
1193 formation of, vertically elongated hydraulic domains such as the porosity waves  
1194 predicted for the decompaction-weakening rheology (Sect. 14.5.6). The greatest  
1195 influence on direction is realized in compression. During tectonic compression, the  
1196 brittle crust supports differential stresses that are approximately twice the lithostatic  
1197 load (Petrini and Podladchikov 2000; Mancktelow 2008). The relaxation of this  
1198 stress gives rise to a negative mean stress gradient that may cause downward  
1199 directed compaction-driven fluid flow on an  $O(l_A)$  scale (Connolly and  
1200 Podladchikov 2004). The inversion also creates a barrier to upward directed  
1201 compaction driven flow. This barrier is most effective within vertically elongated  
1202 hydraulic domains; thus, in contrast to the extensional case, compression may favor  
1203 the formation of slow moving, horizontal, hydraulic domains such as the porosity  
1204 waves predicted for compaction-driven flow in upward strengthening viscous rocks  
1205 (Sect. 14.5.5).

1206 In the lithostatic limit, rocks can sustain fluid overpressures comparable to their  
1207 tensile strength. Thus, decompaction can occur by viscous mechanisms as assumed  
1208 in the porosity wave models presented here. However, in the presence of large  
1209 differential stresses, rocks will fail by plastic mechanisms before the fluid over-  
1210 pressure necessary for viscous dilational mechanisms can develop (Sibson 2000;  
1211 Rozhko et al. 2007). As differential stresses are expected to grow towards the  
1212 brittle-ductile transition, plastic failure will limit the viscous porosity wave mecha-  
1213 nism to greater depths in non-lithostatic settings. Whether truly brittle deformation  
1214 can be propagated upward by viscous compaction at depth, as implied by the  
1215 viscous decompaction-weakening model advocated here, remains to be  
1216 demonstrated.

## 1217 14.7 Concluding Remarks

1218 At near surface conditions, tectonic deformation maintains permeable fracture  
1219 systems that, under most circumstances, permit drainage of crustal fluids with  
1220 negligible fluid overpressure (Zoback and Townend 2001). In this regime, fluid  
1221 flow is largely independent of the stress state of the rock matrix and weak  
1222 perturbations induced by topography or fluid density variations may give rise to  
1223 complex flow patterns (Ingebritsen et al. 2006). The base of the **seismogenic zone**,

at temperatures of  $\sim 623$  K, defines the brittle-ductile transition (Sibson 1986; Scholz 1988), but evidence for the involvement of high pressure fluids in faulting (e.g., Sibson 2009; Cox and Ruming 2004; Miller et al. 2004) indicates that fluid overpressures develop above the brittle-ductile transition on the inter-seismic time scale. This short-term cyclicality reflects the role of localized compaction in sealing faults and fractures (Gratier et al. 2003; Tenthoery and Cox 2006). But at the brittle-ductile transition the time scale for fluid expulsion ( $> 2.3 c_{\sigma} / \dot{\epsilon}_{\text{tectonic}} \sim O(10^8)$  y) is slow with respect to metamorphic fluid production. Thus, the brittle-ductile transition lies within a transitional hydrological regime in which compaction-driven fluid flow is gradually superimposed on the upper crustal regime. Within this transitional regime, the efficiency of compaction increases exponentially with depth on the  $O(1)$  km scale of the viscous e-fold length (Fig. 14.1). But because the efficiency of compaction must be measured relative to rates of fluid production or drainage, it is not possible to make a general statement about the depth or temperature at which metamorphic fluid flow will become dominated by compaction.

Even if recent challenges (e.g., Oliver et al. 2000; Dewey 2005; Ague and Baxter 2007) to the paradigm of heat-conduction limited metamorphism (England and Thompson 1984) are acknowledged, the development of high fluid pressures indicates that metamorphic environments must be characterized by extraordinarily low permeability. Metamorphic fluid expulsion is not necessarily efficient (Warren et al. 2011), but efficient fluid expulsion from poorly drained rocks requires a dynamic mechanism in which the dilational deformation responsible for increasing permeability is balanced by a compaction mechanism at depth responsible for maintaining high fluid pressure. An essential feature of such a mechanism is that, irrespective of the mean-stress gradient, hydraulic connectivity must be maintained over a vertical interval that is large enough to generate the effective pressures necessary to drive the deformation. Both self-propagating domains of fluid-filled fractures (Gold and Soter 1985) and individual hydrofractures (Rubin 1995; Nakashima 1995; Okamoto and Tsuchiya 2009) have been proposed as the mechanism for such flow. These models suppose that the fractures are closed at depth, i.e., compacted, by the elastic response of the matrix. As a consequence, the fractures propagate at high speeds,  $O(1)$  m/s, and have km-scale vertical dimensions. The porosity wave mechanism, reviewed here, may also be manifest as interconnected fractures, provided the individual fractures are small in comparison to the viscous compaction length, but differs from elastic fracture models in that compaction is viscous. A satisfying feature of the viscous mechanism is that it can operate on the grain-scale, thereby explaining the pervasive compaction evident in metamorphic rocks. If viewed as competing mechanisms, the mechanism that requires the smallest vertical extent necessary to accommodate fluid production will dominate. The albeit highly uncertain  $O(100)$  m estimate for the viscous compaction length, obtained here for amphibolite-facies conditions, indicates that porosity waves can meet this criterion for dominance.

The relatively minor role of compaction in many near surface environments makes large scale hydrological modeling of the upper crust possible (Ingebritsen et al. 2006). Possible in this context means that a stable initial condition can be

1269 envisioned in which fluid and rock coexist. In contrast, the lower crust is an  
1270 environment in which fluids are mechanically and, potentially, thermodynamically  
1271 unstable (Connolly and Thompson 1989). Thus there is no time-invariant initial  
1272 condition from which it is possible to assess the impact of the metamorphic process,  
1273 which is itself the most likely source of lower crustal fluids. The assertion that the  
1274 lower crust has an intrinsic **background permeability** towards which transient  
1275 permeability decays is logically specious, because it is based on time-averaged  
1276 metamorphic fluxes. However, permeabilities inferred from time-averaged fluid  
1277 fluxes do provide an upper limit on the background permeability that characterizes  
1278 the local environment of a metamorphic process in time and space (Ingebritsen and  
1279 Manning 2010). The time and length scales for viscous compaction have been  
1280 formulated to emphasize this limitation by separating material properties of the  
1281 solid and fluid, from two transient properties of the initial state, namely porosity and  
1282 the hypothetical background flux necessary to maintain lithostatic fluid pressure. If  
1283 the time-averaged flux is used in place of the background flux, then the result  
1284 provides only upper and lower limits on the compaction length and time scales.  
1285 Consequently, forward models are unlikely to reveal the scales of fluid flow in  
1286 lower crustal systems, but observations of natural patterns may ultimately provide a  
1287 useful parameterization of these scales. These scales are fundamental limits for flow  
1288 phenomena that are independent of stress state within the solid matrix. Thus, the  
1289 scales are constrained by the duration and extent of lateral (e.g., Ferry and Gerdes  
1290 1998; Wing and Ferry 2007; Staude et al. 2009) or downward (e.g., Austrheim  
1291 1987; McCaig et al. 1990; Wickham et al. 1993; Upton et al. 1995; Cartwright and  
1292 Buick 1999; Read and Cartwright 2000; Gleeson et al. 2000; Yardley et al. 2000;  
1293 Munz et al. 2002; Gleeson et al. 2003) fluid flow.

1294 The role of compaction in metamorphic fluid flow is extraordinarily uncertain,  
1295 but ignoring this uncertainty in models of metamorphic fluid flow does not make the  
1296 models any more certain. Compaction is a good news, bad news story. The bad news  
1297 is that the details of lower crustal flow may be influenced by unknowable details.  
1298 The good news is that compaction driven fluid flow has a tendency to self-organize.  
1299 Self-organization eliminates the dependence on details that are present on spatial or  
1300 temporal scales that are smaller than the compaction length and time scales. Porosity  
1301 waves are the mechanism for this self-organization, through which dilational defor-  
1302 mation is localized in either time and/or space to create pathways for fluid expulsion.  
1303 Although, this dilational deformation may be manifest by plastic failure, it is limited  
1304 by the rate of the compaction process necessary to maintain elevated fluid pressures.  
1305 At metamorphic conditions, the compaction process is unequivocally viscous.  
1306 The porosity waves that form in a matrix that compacts by viscous mechanisms  
1307 are generally solitary waves that, once formed, are independent of their source.  
1308 This paper has outlined a simple method of predicting the geometry, size, and speed  
1309 of such waves under the assumption that fluid drainage keeps pace with fluid  
1310 production. If this assumption were true throughout the metamorphic column then  
1311 the time-averaged permeability would be identical to that obtained by assuming  
1312 uniform fluid flow. In fact, the assumption is demonstrably untrue on a crustal scale  
1313 for the viscous case, because the waves slow towards the brittle-ductile transition,

an effect that leads to fluid accumulation. Of course, the activation of other drainage mechanisms may maintain the assumed steady state, but the inconsistency serves to demonstrate that characterizing a dynamic system by a time-averaged dependent property, such as permeability, has no predictive value.

In the viscous limit, the models summarized here predict that lower crustal porosity waves will create fluid-rich horizons, with thickness comparable to  $l_A$ , beneath the brittle-ductile transition (Sect. 14.5.5). Geophysical evidence for such horizons is common (Suetnova et al. 1994; Hammer and Clowes 1996; Ozel et al. 1999; Liotta and Ranalli 1999; Makovsky and Klemperer 1999; Vanyan and Gliko 1999; Stern et al. 2001; Jiracek et al. 2007). Coupled with external forcing, the horizons may function as conduits for the large-scale lateral fluid flow responsible for some types of hydrothermal mineralization and as reservoirs for fluid-driven seismicity (e.g., Cox 2005). Paradoxically, although these horizons reflect upward strengthening of the ductile crust with respect to dilational processes, they may reduce the shear strength of the crust precisely at depths where the crust is presumed to be strong. Fluid flow within this interval of the crust is likely to be further complicated by the influence of tectonic stress developed in the brittle crust (Sect. 14.6.3). To make matters still worse, elastic compaction mechanisms become competitive at this depth (e.g., Fig. 14.15 of Connolly and Podladchikov 1998). Elastic compaction rheology also has wave solutions that form in response to high fluid pressures (Rice 1992), but unlike viscous waves, elastic waves cannot detach from their source and propagate as transient shocks accompanied by fluid pressure surges. Thus, the stagnation of mid-crustal viscous porosity waves may be accompanied by high velocity, low amplitude surges of fluid into the upper crust (Connolly and Podladchikov 1998). This type of flow pattern is consistent with the timing of aftershocks during crustal faulting (Miller et al. 2004). Because elastic waves can propagate through a matrix with no prior hydraulic connectivity, elastic compaction may also be an important mechanism at the onset of metamorphism. Viscoelastic porosity wave solutions exist in the zero-porosity limit (Connolly and Podladchikov 1998), but their relevance to metamorphic fluid expulsion has yet to be explored.

Porosity waves are a mechanism capable of bridging the extremes between pervasive and fully segregated fluid flow. The metasomatic effect of fluid infiltration is maximized between these extremes when the flow is strongly focused into channels, but not fully segregated. A decompaction-weakening matrix rheology, in which the matrix yields more readily under negative effective pressure, than it does under positive pressures, can explain channeling (Sect. 14.5.6). The origin of this rheology is attributed to the asymmetric role of cohesion during dilation (Connolly and Podladchikov 2007). The expression of plastic yielding is temperature-dependent, tending toward the ductile and brittle limits at, respectively, high and low temperatures (Hill 1950). Thus at high temperatures decompaction-weakening is capable of inducing channelized fluid flow in completely ductile rocks (Bouilhol et al. 2011). Reactive transport instability (Daines and Kohlstedt 1994; Aharonov et al. 1997) and shear-enhanced segregation (Holtzman and Kohlstedt 2007) are alternative mechanisms for inducing channelization in ductile rocks. In nature any

1358 mechanism of channelization may be associated with metasomatism, but the  
 1359 reactive transport instability is implicitly metasomatic. A limitation to the reactive  
 1360 transport instability is that the net solubility of the matrix in the fluid must increase  
 1361 in the direction of fluid flow. The key distinction between the flow patterns  
 1362 generated by decompaction-weakening and other focusing mechanisms, is that in  
 1363 the case of decompaction-weakening fluid is circulated into and out of the matrix,  
 1364 whereas reactive transport and shear-enhanced segregation are associated  
 1365 with unidirectional flow. When considered in tandem, mechanical and reactive  
 1366 transport instabilities are mutually reinforcing (Spiegelman et al. 2001; Liang  
 1367 et al. 2010).

1368 **Acknowledgements** This paper was improved by outstanding, although not necessarily lauda-  
 1369 tory, reviews by Stephen F. Cox, Yves Gueguen, Peter O. Koons and Peter I. Nabelek. I am  
 1370 grateful to Dan Harlov and Hakon Austrheim for their extraordinary patience and judicious  
 1371 editing. The work presented here was supported by Swiss National Science Foundation grant  
 1372 200021\_130411.

## 1373 **Appendix: Steady-State Porosity Waves in a Viscous Matrix**

1374 This appendix presents a steady-state wave solution for flow of an incompressible  
 1375 fluid through a viscous matrix composed of incompressible solid grains. Geological  
 1376 compaction literature invariably assumes Newtonian behavior for the viscous  
 1377 mechanism; however, lower crustal environments may well be characterized by  
 1378 power-law viscous rheology (e.g., Kohlstedt et al. 1995). Accordingly, the solution  
 1379 derived here is general with respect to the dependence of the viscous rheology on  
 1380 effective pressure. Aside from this modification, the mathematical formulation of  
 1381 the governing compaction equations is identical to that of Connolly and  
 1382 Podladchikov (2000, 2007).

1383 Conservation of solid and fluid mass requires

$$\frac{\partial(1 - \phi)}{\partial t} + \nabla \cdot ((1 - \phi)\mathbf{v}_s) = 0 \quad (14.35)$$

1384 and

$$\frac{\partial\phi}{\partial t} + \nabla \cdot (\phi\mathbf{v}_f) = 0, \quad (14.36)$$

1385 where subscripts f and s distinguish the velocities,  $\mathbf{v}$ , of the fluid and matrix. From  
 1386 Darcy's law, force balance between the matrix and fluid requires

$$\mathbf{q} = \phi(\mathbf{v}_f - \mathbf{v}_s) = -\frac{k}{\mu}(\nabla p_f - \rho_f \mathbf{g} \mathbf{u}_z). \quad (14.37)$$

no new paragraph

In one-dimensional compaction of a vertical column, mean stress is identical to the load 1387  
1388

no new paragraph

$$\bar{\sigma} = \int_0^z ((1 - \phi)\rho_s + \phi\rho_f)g\mathbf{u}_z dz. \tag{14.38}$$

Thus, in terms of effective pressure,  $p_e = \bar{\sigma} - p_f$ , Eq. 14.37 is 1389

no new paragraph

$$\phi(\mathbf{v}_f - \mathbf{v}_s) = \frac{k}{\mu} (\nabla p_e - (1 - \phi)\Delta\rho g\mathbf{u}_z). \tag{14.39}$$

The divergence of the total volumetric flux of matter is the sum of Eqs. 14.35 and 14.36 1390  
1391

$$\nabla \cdot (\mathbf{v}_s + \phi(\mathbf{v}_f - \mathbf{v}_s)) = 0, \tag{14.40}$$

and substituting Eq. 14.39 into Eq. 14.40 1392

$$\nabla \cdot \left( \mathbf{v}_s + \frac{k}{\mu} (\nabla p_e - (1 - \phi)\Delta\rho g\mathbf{u}_z) \right) = 0. \tag{14.41}$$

← no new paragraph

Matrix rheology is introduced with Eq. 14.16 by observing that the divergence of the solid velocity is the dilational strain rate of the matrix 1393  
1394

$$\nabla \cdot \mathbf{v}_s = \frac{\phi}{1 - \phi} \dot{\epsilon}_\phi = -c_\alpha f_\phi A |p_e|^{n_\sigma - 1} p_e \tag{14.42}$$

where  $f_\phi = \phi(1 - \phi)/(1 - \phi^{1/n_\sigma})^{n_\sigma}$  (Wilkinson and Ashby 1975). As the functional form of Eq. 14.42 may vary depending on the magnitude of the porosity and the viscous mechanism (Ashby 1988), the subsequent analysis assumes  $f_\phi$  is an unspecified function of porosity. 1395  
1396  
1397  
1398

To avoid the unnecessary complication associated with the use of vector notation for a one-dimensional problem, in the remainder of this analysis vector quantities are represented by signed scalars and the gradient and divergence operators are replaced by  $\partial/\partial z$ . Supposing the existence of a steady state solution in which fluid expulsion is accomplished by waves that propagate with unchanging form through a matrix with background porosity  $\phi_0$  filled by fluid at zero effective pressure, then, in a reference frame that travels with the wave, integration of Eq. 14.35 gives the matrix velocity as 1399  
1400  
1401  
1402  
1403  
1404  
1405  
1406

$$v_s = v_\infty \frac{1 - \phi_0}{1 - \phi} \tag{14.43}$$

1407 where  $v_\infty$  is the solid velocity in the limits  $\phi \rightarrow \phi_0$  and  $p_e \rightarrow 0$ , i.e., at infinite  
 1408 distance from the wave. After substitution of Eq. 14.43, the integrated form of  
 1409 Eq. 14.41 can be rearranged to

$$\frac{\partial p_e}{\partial z} = \left( q_t - v_\infty \frac{1 - \phi_0}{1 - \phi} \right) \frac{\mu}{k} + (1 - \phi) \Delta \rho g \quad (14.44)$$

1410 where  $q_t = \phi v_f + (1 - \phi) v_s$  is the constant, total, volumetric flux of matter through  
 1411 the column, which evaluates in the limit  $\phi \rightarrow \phi_0$  and  $p_e \rightarrow 0$  as

$$q_t = v_\infty - (1 - \phi_0) \frac{k_0}{\mu} \Delta \rho g \quad (14.45)$$

1412 where  $k_0$  is the permeability at  $\phi_0$ . Thus, Eq. 14.44 can be rewritten

$$\frac{\partial p_e}{\partial z} = \Delta \rho g \left( 1 - \phi - (1 - \phi_0) \frac{k_0}{k} \right) - v_\infty \frac{\mu}{k} \frac{\phi - \phi_0}{1 - \phi}. \quad (14.46)$$

← no new paragraph

1413 Likewise, substitution of Eq. 14.43 into Eq. 14.42 yields

$$\frac{\partial \phi}{\partial z} = - \frac{(1 - \phi)^2}{1 - \phi_0} f_\phi \frac{c_\sigma A |p_e|^{n_\sigma - 1} p_e}{v_\infty} \quad (14.47)$$

← no new paragraph

1414 If permeability is an, as yet unspecified, function of porosity, then Eqs. 14.46 and  
 1415 14.47 form a closed system of two ordinary differential equations in two unknown  
 1416 functions,  $\phi$  and  $p_e$ . As  $v_\infty$  is the solid velocity at infinite distance from a steady-  
 1417 state wave, if the reference frame is changed to that of the unperturbed matrix, the  
 1418 phase velocity of the wave is  $v_\phi = -v_\infty$ .

1419 For notational simplicity Eqs. 14.46 and 14.47 are rewritten

$$\frac{\partial p_e}{\partial z} = f_1 \quad (14.48)$$

$$\frac{\partial \phi}{\partial z} = f_2 \frac{c_\sigma A}{v_\phi} |p_e|^{n_\sigma - 1} p_e \quad (14.49)$$

1420 where  $f_1$  is the dependence of Eq. 14.46 on  $\phi$  and  $v_\phi$ , and  $f_2$  isolates the dependence  
 1421 of Eq. 14.47 on  $\phi$ . Combining Eqs. 14.48 and 14.49 to eliminate  $z$ , and rearranging,  
 1422 yields

$$0 = \frac{c_\sigma A}{v_\phi} |p_e|^{n_\sigma - 1} p_e dp_e - \frac{f_1}{f_2} d\phi, \quad (14.50)$$

which must be satisfied by the  $\phi$ - $p_e$  trajectory of any steady-state solution. Defining a function  $H$  such that

$$H \equiv - \int \frac{f_1}{f_2} d\phi, \tag{14.51}$$

the integral of Eq. 14.50 yields a function

$$U \equiv \frac{c_\sigma A}{v_\phi} \frac{|p_e|^{n_\sigma - 1} p_e^2}{n_\sigma + 1} + H \tag{14.52}$$

whose  $\phi$ - $p_e$  contours explicitly define the  $\phi$ - $p_e$  trajectory for all steady-state solutions as a function  $v_\phi$ . Because  $U$  increases monotonically, and symmetrically, with positive or negative  $p_e$  at constant  $\phi$ , and  $H$  is independent of  $p_e$ , the stationary points of  $U$  must occur at  $p_e = 0$  and correspond to extrema in  $H$ , i.e., the real roots of  $\partial H / \partial \phi = -f_1 / f_2 = 0$ . Moreover, as  $f_2$  must be finite if the matrix is coherent, the roots of  $\partial H / \partial \phi = 0$  are identical to the roots of  $f_1 = 0$ . Therefore  $\phi_0$  is always a stationary point, with the character of a focal point if  $\partial f_1 / \partial \phi < 0$  and that of a saddle point if  $\partial f_1 / \partial \phi > 0$ . When  $\phi_0$  is a focal point, the steady-state wave solutions correspond to periodic waves that oscillate between two values of porosity on either side of  $\phi_0$ , characterized by equal  $H$ , at which  $p_e$  vanishes (Fig. 14.6b). The case of greater interest is a solitary wave (Fig. 14.6a), in which the porosity rises from  $\phi_0$  to a maximum, at which  $H(\phi_{\max}) = H(\phi_0)$ , and then returns to  $\phi_0$ . This solution requires both the existence of a focal point at  $\phi > \phi_0$  and that  $\phi_0$  is a saddle point. For the rheological constitutive relation employed here (Eq. 14.42), the first condition is always met when  $\phi_0$  is a saddle point. Thus, the critical velocity for the existence of the solitary wave solution, i.e., the bifurcation at which  $\phi_0$  switches from focal to saddle point, is

$$v_\phi^{\text{crit}} = - \frac{k_0}{\mu} (1 - \phi_0) \Delta \rho g \left( \frac{(1 - \phi_0)}{k_0} \frac{\partial k}{\partial \phi} \Big|_{\phi = \phi_0} - 1 \right), \tag{14.53}$$

which is obtained by solving  $\partial f_1 / \partial \phi = 0$  for  $v_\phi$ . Substituting the explicit function for permeability given by Eq. 14.17 into Eq. 14.53 yields

$$v_\phi^{\text{crit}} = - \frac{k_0}{\phi_0 \mu} (1 - \phi_0) \Delta \rho g ((1 - \phi_0) n_\phi - \phi_0) = v_0 ((1 - \phi_0) n_\phi - \phi_0). \tag{14.54}$$

← no new paragraph

Equation 14.54 implies that, in the small-porosity limit, the minimum speed at which steady solitary waves exist is  $n_\phi$  times the speed of the fluid through the unperturbed matrix.

The relation between amplitude (maximum porosity) and  $v_\phi$  is obtained by solving

$$H(\phi_{\max}) - H(\phi_0) = - \int_{\phi_0}^{\phi_{\max}} \frac{f_1}{f_2} d\phi = 0. \tag{14.55}$$

no new paragraph

1450 The resulting expressions are cumbersome, but, in the small-porosity limit of 1451 Eqs. 14.17 and 14.42, the solution of Eq. 14.55 is

$$v_\phi = - \frac{c_\phi \phi_0^{n_\phi - 1} \Delta \rho g}{\mu} (n_\phi - 1) \frac{\phi_0^{n_\phi} + \phi_{\max}^{n_\phi} \left[ n_\phi \ln \left( \frac{\phi_{\max}}{\phi_0} \right) - 1 \right]}{\phi_0^{n_\phi - 1} [n_\phi \phi_{\max} - \phi_0 (n_\phi - 1)] - \phi_{\max}^{n_\phi}}. \tag{14.56}$$

no new paragraph

1452 From Eq. 14.56 it follows that  $n_\phi > 1$  is a necessary condition for the existence 1453 of solitary waves. Equation 14.56 also has the surprising implication that amplitude 1454 is not a function of  $n_\sigma$ , for large porosity the function  $f_\phi$ , in the exact form of 1455 Eq. 14.42, gives rise to a weak dependence of amplitude on  $n_\sigma$ . For a solitary wave 1456 with specified phase velocity, the effective pressure is obtained as an explicit 1457 function of  $\phi$  from the definite integral of Eq. 14.50, which can be rearranged to

$$p_e = \pm \sqrt[n_\sigma + 1]{(n_\sigma + 1) \frac{v_\phi}{c_\sigma A} \int_{\phi_0}^{\phi} \frac{f_1}{f_2} d\phi}, \tag{14.57}$$

1458 where the signs have been dropped in view of the symmetry of the solution. And 1459 finally, substituting Eq. 14.57 into Eq. 14.47, inverting the result, and integrating 1460 yields the depth coordinate relative to the center of a wave as a function of  $\phi$

$$z = \pm \sqrt[n_\sigma + 1]{\frac{v_\phi}{c_\sigma A (n_\sigma + 1)^{n_\sigma}} \int_{\phi_{\max}}^{\phi} \frac{1}{f_2} \left( \int_{\phi_0}^{\phi} \frac{f_1}{f_2} d\phi \right)^{-\frac{n_\sigma}{n_\sigma + 1}} d\phi}. \tag{14.58}$$

no new paragraph

1461 To demonstrate that  $z \rightarrow \pm\infty$  as  $\phi \rightarrow \phi_0$ , the inner integral and its factor in 1462 Eq. 14.58 are approximated by the first non-zero terms of Taylor series expansions 1463 about  $\phi = \phi_0$  to obtain

$$z \approx \pm \left( \frac{v_\phi}{c_\sigma A f_2|_{\phi=\phi_0}} \left( \frac{n_\sigma + 1}{2} \frac{\partial f_1}{\partial \phi} \Big|_{\phi=\phi_0} \right)^{-n_\sigma} \right)^{\frac{1}{n_\sigma + 1}} \int_{\phi}^0 \Phi^{-\frac{2n_\sigma}{n_\sigma + 1}} d\Phi \tag{14.59}$$

1464 where  $\Phi = \phi - \phi_0$ . In the limit  $\Phi \rightarrow 0$ , the integral in Eq. 14.59 is finite only if 1465  $n_\sigma < 1$ , from which it is concluded that solitary waves have infinite wavelength in a 1466 linear or shear thinning viscous matrix, but may have finite wavelength in the 1467 peculiar case of a shear thickening viscous matrix. Rewriting the integral in 1468 Eq. 14.59 in terms of  $\ln \phi$ , and differentiating yields

$$\frac{\partial z}{\partial \ln \Phi} \approx \left( \Phi^{1-n_\sigma} \frac{v_\phi}{c_\sigma A f_2|_{\phi=\phi_0}} \left( \frac{n_\sigma + 1}{2} \frac{\partial f_1}{\partial \phi} \Big|_{\phi=\phi_0} \right)^{-n_\sigma} \right)^{\frac{1}{n_\sigma+1}} \quad (14.60)$$

the depth interval over which porosity decays from  $e\phi_0$  to  $\phi_0$  within a porosity 1469  
wave. This interval is taken here as the characteristic length scale for variations in 1470  
porosity, i.e., the viscous compaction length. The derivative on the left-hand side of 1471  
Eq. 14.60, 1472

$$\frac{\partial f_1}{\partial \phi} \Big|_{\phi=\phi_0} = \Delta \rho g \left( \frac{(1-\phi_0)}{k_0} \frac{\partial k}{\partial \phi} \Big|_{\phi=\phi_0} - 1 \right) + \frac{v_\phi \mu}{k_0(1-\phi_0)}, \quad (14.61)$$

is zero at  $v_\phi = v_\phi^{\text{crit}}$ , but decreases monotonically with  $v_\phi$ ; thus dropping the first 1473  
term in Eq. 14.61, and substituting  $v_\phi = v_\phi^{\text{crit}}$  and  $\Phi = (e-1)\phi_0$  in Eq. 14.60, and 1474  
expanding  $f_2$  at  $\phi_0$  as  $(1-\phi_0)f_\phi|_{\phi=\phi_0}$  yields 1475

$$\delta = \left[ \left( (e-1)\phi_0 \Delta \rho g \left( [1-\phi_0] \frac{\partial k}{\partial \phi} \Big|_{\phi=\phi_0} - k_0 \right) \right)^{1-n_\sigma} \left( \frac{2k_0}{n_\sigma+1} \right)^{n_\sigma} \frac{1}{c_\sigma A \mu f_\phi|_{\phi=\phi_0}} \right]^{\frac{1}{n_\sigma+1}}, \quad (14.62)$$

a length scale that provides a lower bound on wavelength. For a linear-viscous 1476  
matrix with shear viscosity  $\eta = 1/(3A)$ , the constitutive relation given by 1477  
Eq. 14.42, and the small-porosity limit, Eq. 14.62 simplifies to 1478

$$\delta = \sqrt{\frac{4}{3} \frac{\eta}{\phi_0} \frac{k_0}{\mu}}$$

which, accounting for differences in the formulation of the bulk viscosity of the 1479  
matrix, is identical to the viscous compaction length of McKenzie (1984). For a 1480  
non-linear viscous matrix, making use of constitutive relations given by Eqs. 14.17 1481  
and 14.42, in the small-porosity limit the compaction length is 1482

$$\delta = C \phi_0^{\frac{n_\sigma-1}{n_\sigma+1}} \sqrt{\left( \frac{2}{n_\sigma+1} \right)^{n_\sigma} \frac{c_\phi}{c_\sigma A \mu (\Delta \rho g)^{n_\sigma-1}}}, \quad (14.63)$$

where 1483

$$C = \sqrt[n_\sigma+1]{[n_\phi(e-1)]^{1-n_\sigma}}. \quad (14.64)$$

1484 The factor  $C$  represents two non-general assumptions of the analysis: that the  
 1485 phase velocity is  $n_\phi v_0$ ; and that the porosity decay is from  $e\phi_0$  to  $\phi_0$ . In the spirit of  
 1486 dimensional analysis, this factor ( $\sim 2.27$  for  $n_\sigma = n_\phi = 3$ ) is neglected in the text.

## 1487 References

AU3

- 1488 Ague JJ, Baxter EF (2007) Brief thermal pulses during mountain building recorded by Sr diffusion  
 1489 in apatite and multicomponent diffusion in garnet. *Earth Planet Sci Lett* 261:500–516.  
 1490 doi:10.1016/j.epsl.2007.07.017
- 1491 Ague JJ, Park J, Rye DM (1998) Regional metamorphic dehydration and seismic hazard. *Geophys*  
 1492 *Res Lett* 25:4221–4224
- 1493 Aharonov E, Spiegelman M, Kelemen P (1997) Three-dimensional flow and reaction in porous  
 1494 media: implications for the earth's mantle and sedimentary basins. *J Geophys Res*  
 1495 102:14821–14833
- 1496 Ashby MF (1988) The modeling of hot isostatic pressing. In: Garvare T (ed) *Proceedings hip: hot*  
 1497 *isostatic pressing – theories and applications*. Centek, Lulea, pp 29–40
- 1498 Athy LF (1930) Density, porosity and compaction of sedimentary rocks. *Bull Am Assoc Pet Geol*  
 1499 14:1–24
- 1500 Austrheim H (1987) Eclogitization of lower crustal granulites by fluid migration through shear  
 1501 zones. *Earth Planet Sci Lett* 81:221–232. doi:10.1016/0012-821X(87)90158-0
- ~~1502 Balashov VN, Yardley BWD (1998) Modeling metamorphic fluid flow with reaction-compaction-~~  
~~1503 permeability feedbacks. *Am J Sci* 298:441–470~~
- 1504 Barcilon V, Lovera OM (1989) Solitary waves in magma dynamics. *J Fluid Mech* 204:121–133
- 1505 Barcilon V, Richter FM (1986) Nonlinear waves in compacting media. *J Fluid Mech* 164:429–448
- 1506 Bercovici D, Ricard Y, Schubert G (2001) A two-phase model for compaction and damage 1.  
 1507 General theory. *J Geophys Res* 106:8887–8906
- 1508 Bouilhol P, Burg JP, Bodinier JL, Schmidt MW, Dawood H, Hussain S (2009) Magma and fluid  
 1509 percolation in arc to forearc mantle: evidence from Sapat (Kohistan, Northern Pakistan). *Lithos*  
 1510 107:17–37. doi:10.1016/j.lithos.2008.07.004
- 1511 Bouilhol P, Connolly JAD, Burg JP (2011) Geological evidence and modeling of melt migration  
 1512 by porosity waves in the sub-arc mantle of Kohistan (Pakistan). *Geology* 39:1091–1094.  
 1513 doi:10.1130/G32219.1
- 1514 Cartwright I, Buick IS (1999) The flow of surface-derived fluids through alic springs age middle-  
 1515 crustal ductile shear zones, Reynolds Range, Central Australia. *J Metamorph Geol* 17:397–414
- 1516 Cheadle MJ, Elliott MT, McKenzie D (2004) Percolation threshold and permeability of  
 1517 crystallizing igneous rocks: the importance of textural equilibrium. *Geology* 32:757–760.  
 1518 doi:10.1130/g20495.1
- 1519 Connolly JAD (1997) Devolatilization-generated fluid pressure and deformation-propagated fluid  
 1520 flow during prograde regional metamorphism. *J Geophys Res* 102:18149–18173
- 1521 Connolly JAD (2010) The mechanics of metamorphic fluid expulsion. *Elements* 6:165–172.  
 1522 doi:10.2113/gselements.6.3.165
- 1523 Connolly JAD, Podladchikov YY (1998) Compaction-driven fluid flow in viscoelastic rock.  
 1524 *Geodinamica Acta* 11:55–84
- 1525 Connolly JAD, Podladchikov YY (2000) Temperature-dependent viscoelastic compaction and  
 1526 compartmentalization in sedimentary basins. *Tectonophysics* 324:137–168
- 1527 Connolly JAD, Podladchikov YY (2004) Fluid flow in compressive tectonic settings: implications  
 1528 for mid-crustal seismic reflectors and downward fluid migration. *J Geophys Res* 109:B04201.  
 1529 doi:10.1029/2003JB002822

- Connolly JAD, Podladchikov YY (2007) Decompaction weakening and channeling instability in ductile porous media: implications for asthenospheric melt segregation. *J Geophys Res* 112: B10205. doi:10.1029/2005jb004213 1530-1532
- Connolly JAD, Thompson AB (1989) Fluid and enthalpy production during regional metamorphism. *Contrib Mineral Petrol* 102:346–366 1533-1534
- Connolly JAD, Schmidt MW, Solferino G, Bagdassarov N (2009) Permeability of asthenospheric mantle and melt extraction rates at mid-ocean ridges. *Nature* 462:209–212. doi:10.1038/nature08517 1535-1537
- Cox SF (2005) Coupling between deformation, fluid pressures and fluid flow in ore-producing hydrothermal environments. In: *Economic geology 100th anniversary volume*, Denver, pp 39–75 1538-1540
- Cox SF, Ruming K (2004) The St Ives mesothermal gold system, Western Australia – a case of golden aftershocks? *J Struct Geol* 26:1109–1125. doi:10.1016/j.jsg.2003.11.025 1541-1542
- Daines MJ, Kohlstedt DL (1994) The transition from porous to channelized flow due to melt/rock reaction during melt migration. *Geophys Res Lett* 21:145–148 1543-1544
- Dewey JF (2005) Orogeny can be very short. *Proc Natl Acad Sci USA* 102:15286–15293. doi:10.1073/pnas.0505516102 1545-1546
- England PC, Thompson AB (1984) Pressure temperature time paths of regional metamorphism. 1. Heat-transfer during the evolution of regions of thickened continental-crust. *J Petrol* 25:894–928 1547-1549
- Etheridge MA, Wall VJ, Cox SF, Vernon RH (1984) High fluid pressures during regional metamorphism and deformation – implications for mass-transport and deformation mechanisms. *J Geophys Res* 89:4344–4358 1550-1552
- Ferry JM (1994) Overview of the petrologic record of fluid-flow during regional metamorphism in Northern New-England. *Am J Sci* 294:905–988 1553-1554
- Ferry JM, Gerdes ML (1998) Chemically reactive fluid flow during metamorphism. *Annu Rev Earth Planet Sci* 26:255–287 1555-1556
- Fulton PM, Saffer DM, Bekins BA (2009) A critical evaluation of crustal dehydration as the cause of an overpressured and weak San Andreas Fault. *Earth Planet Sci Lett* 284:447–454. doi:10.1016/j.epsl.2009.05.009 1557-1559
- Gavrilenko P, Gueguen Y (1993) Fluid overpressures and pressure solution in the crust. *Tectonophysics* 21:91–110 1560-1561
- Gleeson SA, Yardley BWD, Boyce AJ, Fallick AE, Munz LA (2000) From basin to basement: the movement of surface fluids into the crust. *J Geochem Explor* 69:527–531 1562-1563
- Gleeson SA, Yardley BWD, Munz IA, Boyce AJ (2003) Infiltration of basinal fluids into high-grade basement, South Norway: sources and behaviour of waters and brines. *Geofluids* 3:33–48 1564-1565
- Gold T, Soter S (1985) Fluid ascent through the solid lithosphere and its relation to earthquakes. *Pure Appl Geophys* 122:492–530 1566-1567
- Goldschmidt VM (1954) *Geochemistry*. Clarendon, Oxford, p 730 1568
- Graham CM, Valley JW, Eiler JM, Wada H (1998) Timescales and mechanisms of fluid infiltration in a marble: an ion microprobe study. *Contrib Mineral Petrol* 132:371–389 1569-1570
- Gratier JP, Favreau P, Renard F (2003) Modeling fluid transfer along California faults when integrating pressure solution crack sealing and compaction processes. *J Geophys Res* 108. doi:10.1029/2001jb000380 1571-1573
- Gueguen Y, Palciauskas VV (1994) *Introduction to the physics of rocks*. Princeton University Press, Princeton, p 194 1574-1575
- Gueguen Y, Dormieux L, Bouteca M (2004) Fundamentals of poromechanics. In: Gueguen Y, Bouteca M (eds) *Mechanics of fluid-saturated rocks*. Elsevier Academic, Burlington, pp 55–79 1576-1577
- Hammer PTC, Clowes RM (1996) Seismic reflection investigations of the mount caley bright spot: a midcrustal reflector beneath the Coast Mountains, British Columbia. *J Geophys Res* 101:20119–20131 1578-1580
- Hanson RB (1997) Hydrodynamics of regional metamorphism due to continental collision. *Econ Geol Bull Soc Econ Geol* 92:880–891 1581-1582

- 1583 Hetenyi G, Cattin R, Brunet F, Bollinger L, Vergne J, Nabelek J, Diament M (2007) Density  
1584 distribution of the India plate beneath the Tibetan Plateau: geophysical and petrological  
1585 constraints on the kinetics of lower-crustal eclogitization. *Earth Planet Sci Lett* 264:226–244.  
1586 doi:10.1016/j.epsl.2007.09.036
- 1587 Hill R (1950) *The mathematical theory of plasticity*. Clarendon, Oxford, p 356
- 1588 Holness MB, Siklos STC (2000) The rates and extent of textural equilibration in high-temperature  
1589 fluid-bearing systems. *Chem Geol* 162:137–153. doi:10.1016/S0009-2541(99)00124-2
- 1590 Holtzman BK, Kohlstedt DL (2007) Stress-driven melt segregation and strain partitioning  
1591 in partially molten rocks: effects of stress and strain. *J Petrol* 48:2379–2406.  
1592 doi:10.1093/petrology/egm065
- 1593 Huenges E, Erzinger J, Kuck J, Engeser B, Kessels W (1997) The permeable crust: geohydraulic  
1594 properties down to 9101 m depth. *J Geophys Res* 102:18255–18265
- 1595 Hunt JM (1990) Generation and migration of petroleum from abnormally pressured fluid  
1596 compartments. *Am Assoc Pet Geol* 74:1–12
- 1597 Ingebritsen SE, Manning CE (1999) Geological implications of a permeability-depth curve for the  
1598 continental crust. *Geology* 27:1107–1110
- 1599 Ingebritsen SE, Manning CE (2010) Permeability of the continental crust: dynamic variations  
1600 inferred from seismicity and metamorphism. *Geofluids* 10:193–205. doi:10.1111/j.1468-  
1601 8123.2010.00278.x
- 1602 Ingebritsen SE, Sanford WE, Neuzil C (2006) *Groundwater in geologic processes*. Cambridge  
1603 University Press, Cambridge
- 1604 Jagoutz O, Muntener O, Burg JP, Ulmer P, Jagoutz E (2006) Lower continental crust formation  
1605 through focused flow in km-scale melt conduits: the zoned ultramafic bodies of the Chilas  
1606 complex in the Kohistan Island Arc (NW Pakistan). *Earth Planet Sci Lett* 242:320–342
- 1607 Jiracek GR, Gonzalez VM, Caldwell TG, Wannamaker PE, Kilb D (2007) Seismogenic, electrically  
1608 conductive, and fluid zones at continental plate boundaries in New Zealand, Himalaya,  
1609 and California-USA. *Geophys Monogr Ser* 175:347–369. doi:10.1029/175GM18
- 1610 Kerschhofer L, Dupas C, Liu M, Sharp TG, Durham WB, Rubie DC (1998) Polymorphic  
1611 transformations between olivine, wadsleyite and ringwoodite: mechanisms of intracrystalline  
1612 nucleation and the role of elastic strain. *Mineral Mag* 62:617–638
- 1613 Kohlstedt DL, Evans B, Mackwell SJ (1995) Strength of the lithosphere – constraints imposed by  
1614 laboratory experiments. *J Geophys Res* 100:17587–17602
- 1615 Liang Y, Schiemenz A, Hesse MA, Parmentier EM, Hesthaven JS (2010) High-porosity channels  
1616 for melt migration in the mantle: top is the dunite and bottom is the harzburgite and lherzolite.  
1617 *Geophys Res Lett* 37:L15306. doi:10.1029/2010gl044162
- 1618 Liotta D, Ranalli G (1999) Correlation between seismic reflectivity and rheology in extended  
1619 lithosphere: southern Tuscany, Inner Northern Apennines, Italy. *Tectonophysics* 315:109–122
- 1620 Makovsky Y, Klemperer SL (1999) Measuring the seismic properties of Tibetan bright spots:  
1621 evidence for free aqueous fluids in the Tibetan middle crust. *J Geophys Res* 104:10795–10825
- 1622 Mancktelow NS (2008) Tectonic pressure: theoretical concepts and modelled examples. *Lithos*  
1623 103:149–177. doi:10.1016/j.lithos.2007.09.013
- 1624 Manning CE, Ingebritsen SE (1999) Permeability of the continental crust: implications of geo-  
1625 thermal data and metamorphic systems. *Rev Geophys* 37:127–150
- 1626 McCaig AM, Wickham SM, Taylor HP (1990) Deep fluid circulation in alpine shear zones,  
1627 Pyrenees, France – field and oxygen isotope studies. *Contrib Mineral Petrol* 106:41–60
- 1628 McCuaig TC, Kerrich R (1998) P-T-t-deformation-fluid characteristics of lode gold deposits:  
1629 evidence from alteration systematics. *Ore Geol Rev* 12:381–453
- 1630 McKenzie D (1984) The generation and compaction of partially molten rock. *J Petrol* 2:713–765
- 1631 Milke R, Abart R, Kunze K, Koch-Müller M, Schmid D, Ulmer P (2009) Matrix rheology effects  
1632 on reaction rim growth I: evidence from orthopyroxene rim growth experiments. *J Metamorph*  
1633 *Geol* 27:71–82. doi:10.1111/j.1525-1314.2008.00804.x
- 1634 Miller SA, Collettini C, Chiaraluce L, Cocco M, Barchi M, Kaus BJP (2004) Aftershocks driven  
1635 by a high-pressure CO<sub>2</sub> source at depth. *Nature* 427:724–727. doi:10.1038/nature02251

- Mosenfelder JL, Connolly JAD, Rubie DC, Liu M (2000) Strength of (Mg, Fe)<sub>2</sub>SiO<sub>4</sub> wadsleyite determined by relaxation of transformation stress. *Phys Earth Planet Inter* 120:63–78 1636
- Munz IA, Yardley BWD, Gleeson SA (2002) Petroleum infiltration of high-grade basement, South Norway: pressure-temperature-time-composition (P-T-t-X) constraints. *Geofluids* 2:41–53 1639
- Nabelek PI (2009) Numerical simulation of kinetically-controlled calc-silicate reactions and fluid flow with transient permeability around crystallizing plutons. *Am J Sci* 309:517–548. doi:10.2475/07.2009.01 1640
- Nakashima Y (1995) Transport model of buoyant metamorphic fluid by hydrofracturing in leaky rock. *J Metamorph Geol* 13:727–736 1643
- Neuzil CE (1994) How permeable are clays and shales? *Water Resour Res* 30:145–150 1645
- Norton D, Knapp R (1977) Transport phenomena in hydrothermal systems – nature of porosity. *Am J Sci* 277:913–936 1647
- Okamoto A, Tsuchiya N (2009) Velocity of vertical fluid ascent within vein-forming fractures. *Geology* 37:563–566. doi:10.1130/g25680a.1 1649
- Oliver GJH, Chen F, Buchwaldt R, Hegner E (2000) Fast tectonometamorphism and exhumation in the type area of the Barrovian and Buchan zones. *Geology* 28:459–462 1650
- Ozel O, Iwasaki T, Moriya T, Sakai S, Maeda T, Piao C, Yoshii T, Tsukada S, Ito A, Suzuki M, Yamazaki A, Miyamachi H (1999) Crustal structure of Central Japan and its petrological implications. *Geophys J Int* 138:257–274 1653
- Padron-Navarta JA, Tommasi A, Garrido CJ, Sanchez-Vizcaino VL, Gomez-Pugnaire MT, Jabaloy A, Vauchez A (2010) Fluid transfer into the wedge controlled by high-pressure hydrofracturing in the cold top-slab mantle. *Earth Planet Sci Lett* 297:271–286. doi:10.1016/j.epsl.2010.06.029 1656
- Padron-Navarta JA, Sanchez-Vizcaino VL, Garrido CJ, Gomez-Pugnaire MT (2011) Metamorphic record of high-pressure dehydration of antigorite serpentinite to chlorite harzburgite in a subduction setting (Cerro del Almiraz, Nevado-Filabride Complex, Southern Spain). *J Petrol* 52:2047–2078. doi:10.1093/petrology/egr039 1662
- Paterson MS, Luan FC (1990) Quartzite rheology under geological conditions. In: Knipe RJ, Rutter EH (eds) *Deformation mechanisms, rheology and tectonics*, vol 54. The Geological Society, London, pp 299–307 1665
- Peng ZG, Vidale JE, Creager KC, Rubinstein JL, Gombert J, Bodin P (2008) Strong tremor near Parkfield, CA, excited by the 2002 Denali fault earthquake. *Geophys Res Lett* 35. doi:10.1029/2008gl036080 1666
- Petrini K, Podladchikov Y (2000) Lithospheric pressure-depth relationship in compressive regions of thickened crust. *J Metamorph Geol* 18:67–78 1670
- Plank T, Langmuir CH (1998) The chemical composition of subducting sediment and its consequences for the crust and mantle. *Chem Geol* 145:325–394 1672
- Powley DE (1990) Pressures and hydrogeology in petroleum basins. *Earth Sci Rev* 29:215–226 1673
- Price JD, Wark DA, Watson EB, Smith AM (2006) Grain-scale permeabilities of faceted polycrystalline aggregates. *Geofluids* 6:302–318. doi:10.1111/j.1468-8123.2006.00149.x 1674
- Ranalli G (1995) *Rheology of the earth*. Springer, New York 1676
- Ranalli G, Rybach L (2005) Heat flow, heat transfer and lithosphere rheology in geothermal areas: features and examples. *J Volcanol Geotherm Res* 148:3–19. doi:10.1016/j.jvolgeores.2005.04.010 1677
- Read CM, Cartwright I (2000) Meteoric fluid infiltration in the middle crust during shearing: examples from the Arunta Inlier, Central Australia. *J Geochem Explor* 69:333–337 1680
- Rice JR (1992) Fault stress states, pore pressure distributions, and the weakness of the San Andreas Fault. In: Evans B, Wong T-F (eds) *Fault mechanics and transport properties of rocks*. Academic, New York, pp 475–503 1683
- Richter FM, McKenzie D (1984) Dynamical models for melt segregation from a deformable rock matrix. *J Geol* 92:729–740 1685
- Rozhko AY, Podladchikov YY, Renard F (2007) Failure patterns caused by localized rise in pore-fluid overpressure and effective strength of rocks. *Geophys Res Lett* 34:L22304. doi:10.1029/2007gl031696 1688

- 1689 Rubie DC, Thompson AB (1985) Kinetics of metamorphic reactions. In: Thompson AB, Rubie DC  
1690 (eds) *Metamorphic reactions kinetics, textures, and deformation*, vol 4. Springer, New York,  
1691 pp 291
- 1692 Rubin RM (1995) Propagation of magma-filled cracks. *Annu Rev Earth Planet Sci* 23:287–336
- 1693 Rubinstein JL, Vidale JE, Gomberg J, Bodin P, Creager KC, Malone SD (2007) Non-volcanic  
1694 tremor driven by large transient shear stresses. *Nature* 448:579–582. doi:10.1038/nature06017
- 1695 Rutter EH (1983) Pressure solution in nature, theory and experiment. *J Geol Soc Lond*  
1696 140:725–740
- 1697 Scarpa R, Amoroso A, Crescentini L, Fischione C, Formisano LA, La Rocca M, Tronca F (2008)  
1698 Slow earthquakes and low frequency tremor along the Apennines, Italy. *Ann Geophys*  
1699 51:527–538
- 1700 Schmalholz SM, Podladchikov Y (1999) Buckling versus folding: importance of viscoelasticity.  
1701 *Geophys Res Lett* 26:2641–2644
- 1702 Scholz CH (1988) The brittle-plastic transition and the depth of seismic faulting. *Geol Rundsch*  
1703 77:319–328
- 1704 Scott DR (1988) The competition between percolation and circulation in a deformable porous-  
1705 medium. *J Geophys Res* 93:6451–6462
- 1706 Scott DR, Stevenson DJ (1986) Magma ascent by porous flow. *J Geophys Res* 91:9283–9296
- 1707 Scott DR, Stevenson DJ, Whitehead JA (1986) Observations of solitary waves in a viscously  
1708 deformable pipe. *Nature* 319:759–761
- 1709 Shaw DM (1956) Geochemistry of pelite rocks, iii, major elements and general geochemistry.  
1710 *Geol Soc Am Bull* 67:919–934
- 1711 Shimizu I (1995) Kinetics of pressure solution creep in quartz; theoretical considerations.  
1712 *Tectonophysics* 245:121–134
- 1713 Sibson RH (1986) Earthquakes and rock deformation in crustal fault zones. *Annu Rev Earth Planet*  
1714 *Sci* 14:149–175
- 1715 Sibson RH (1992) Fault-valve behavior and the hydrostatic lithostatic fluid pressure interface.  
1716 *Earth Sci Rev* 32:141–144
- 1717 Sibson RH (2000) Tectonic controls on maximum sustainable overpressure: fluid redistribution  
1718 from stress transitions. *J Geochem Explor* 69:471–475
- 1719 Sibson RH (2004) Controls on maximum fluid overpressure defining conditions for mesozonal  
1720 mineralisation. *J Struct Geol* 26:1127–1136. doi:10.1016/j.jsg.2003.11.003
- 1721 Sibson RH (2009) Rupturing in overpressured crust during compressional inversion—the case from  
1722 NE Honshu, Japan. *Tectonophysics* 473:404–416. doi:10.1016/j.tecto.2009.03.016
- 1723 Simpson GDH (1998) Dehydration-related deformation during regional metamorphism, NW  
1724 Sardinia, Italy. *J Metamorph Geol* 16:457–472
- 1725 Skelton ADL (1996) The timing and direction of metamorphic fluid flow in Vermont. *Contrib*  
1726 *Mineral Petrol* 125:75–84
- 1727 Skelton ADL, Valley JW, Graham CM, Bickle MJ, Fallick AE (2000) The correlation of reaction  
1728 and isotope fronts and the mechanism of metamorphic fluid flow. *Contrib Mineral Petrol*  
1729 138:364–375
- 1730 Spiegelman M (1993) Flow in deformable porous-media. 1. Simple analysis. *J Fluid Mech*  
1731 247:17–38
- 1732 Spiegelman M, Elliott T (1993) Consequences of melt transport for uranium series disequilibrium  
1733 in young lavas. *Earth Planet Sci Lett* 118:1–20
- 1734 Spiegelman M, Kelemen PB, Aharonov E (2001) Causes and consequences of flow organization  
1735 during melt transport: the reaction infiltration instability in compactible media. *J Geophys Res*  
1736 106:2061–2077
- 1737 Spiers CJ, Schutjens PMTM (1990) Densification of crystalline aggregates by diffusional creep.  
1738 *J Geolo Soc Spec Publ* 54:215–227
- 1739 Stahle HJ, Raith M, Hoernes S, Delfs A (1987) Element mobility during incipient granulite  
1740 formation at kabbaldurga, Southern India. *J Petrol* 28:803–834

- Stauda S, Bons PD, Markl G (2009) Hydrothermal vein formation by extension-driven dewatering of the middle crust: an example from SW Germany. *Earth Planet Sci Lett* 286:387–395. doi:10.1016/j.epsl.2009.07.012 1741–1743
- Stern T, Kleffmann S, Okaya D, Scherwath M, Bannister S (2001) Low seismic-wave speeds and enhanced fluid pressure beneath the Southern Alps of New Zealand. *Geology* 29:679–682 1744–1745
- Stevenson D (1989) Spontaneous small-scale melt segregation in partial melts undergoing deformation. *Geophys Res Lett* 16:1067–1070 1746–1747
- Suetnova EI, Carbonell R, Smithson SB (1994) Bright seismic reflections and fluid movement by porous flow in the lower crust. *Earth Planet Sci Lett* 126:161–169. doi:10.1016/0012-821x(94)90248-8 1748–1750
- Sumita I, Yoshida S, Kumazawa M, Hamano Y (1996) A model for sedimentary compaction of a viscous medium and its application to inner-core growth. *Geophys J Int* 124:502–524 1751–1752
- Tenthorey E, Cox SF (2006) Cohesive strengthening of fault zones during the interseismic period: an experimental study. *J Geophys Res* 111:B09202. doi:10.1029/2005jb004122 1753–1754
- Thompson AB, Connolly JAD (1990) Metamorphic fluids and anomalous porosities in the lower crust. *Tectonophysics* 182:47–55 1755–1756
- Tumarkina E, Misra S, Burlini L, Connolly JAD (2011) An experimental study of the role of shear deformation on partial melting of a synthetic metapelite. *Tectonophysics* 503:92–99. doi:10.1016/j.tecto.2010.12.004 1757–1759
- Upton P, Koons PO, Chamberlain CP (1995) Penetration of deformation-driven meteoric water into ductile rocks: isotopic and model observations from the Southern Alps, New Zealand. *N Z J Geol Geophys* 38:535–543 1760–1762
- van Haren JLM, Ague JJ, Rye DM (1996) Oxygen isotope record of fluid infiltration and mass transfer during regional metamorphism of pelitic schist, Connecticut, USA. *Geochim et Cosmochim Acta* 60:3487–3504 1763–1765
- Vanyan LL, Gliko AO (1999) Seismic and electromagnetic evidence of dehydration as a free water source in the reactivated crust. *Geophys J Int* 137:159–162 1766–1767
- Vrijmoed JC, Podladchikov YY, Andersen TB, Hartz EH (2009) An alternative model for ultra-high pressure in the Svartberget Fe-Ti Garnet-Peridotite, Western Gneiss Region, Norway. *Eur J Mineral* 21:1119–1133. doi:10.1127/0935-1221/2009/0021-1985 1768–1770
- Walther JV, Orville PM (1982) Volatile production and transport in regional metamorphism. *Contrib Mineral Petrol* 79:252–257 1771–1772
- Wark DA, Watson EB (1998) Grain-scale permeabilities of texturally equilibrated, monomineralic rocks. *Earth Planet Sci Lett* 164:591–605 1773–1774
- Warren CJ, Smye AJ, Kelley SP, Sherlock SC (2011) Using white mica  $^{40}\text{Ar}/^{39}\text{Ar}$  data as a tracer for fluid flow and permeability under high-p conditions: Tauern Window, Eastern Alps. *J Metamorph Geol*. doi:10.1111/j.1525-1314.2011.00956.x 1775–1777
- Wickham SM, Peters MT, Fricke HC, Oneil JR (1993) Identification of magmatic and meteoric fluid sources and upward-moving and downward-moving infiltration fronts in a metamorphic core complex. *Geology* 21:81–84 1778–1779
- Wiggins C, Spiegelman M (1995) Magma migration and magmatic solitary waves in 3-d. *Geophys Res Lett* 22:1289–1292 1781–1782
- Wilkinson DS, Ashby MF (1975) Pressure sintering by power law creep. *Acta Metall* 23:1277–1285 1783–1784
- Wing BA, Ferry JM (2007) Magnitude and geometry of reactive fluid flow from direct inversion of spatial patterns of geochemical alteration. *Am J Sci* 307:793–832. doi:10.2475/05.2007.02 1785–1786
- Wong TF, Christian D, Menendez B (2004) Mechanical compaction. In: Gueguen Y, Bouteica M (eds) *Mechanics of fluid-saturated rocks*. Elsevier Academic, Burlington, pp 55–79 1787–1788
- Xiao XH, Evans B, Bernabe Y (2006) Permeability evolution during non-linear viscous creep of calcite rocks. *Pure Appl Geophys* 163:2071–2102. doi:10.1007/s00024-006-0115-1 1789–1790
- Yardley BWD (1983) Quartz veins and devolatilization during metamorphism. *J Geol Soc* 140:657–663 1791–1792

- 1793 Yardley B, Gleeson S, Bruce S, Banks D (2000) Origin of retrograde fluids in metamorphic rocks.  
1794 J Geochem Explor 69:281–285
- 1795 Young ED, Rumble D (1993) The origin of correlated variations in insitu  $O^{18}/O^{16}$  and elemental  
1796 concentrations in metamorphic garnet from southeastern Vermont, USA. Geochim et  
1797 Cosmochim Acta 57:2585–2597. doi:10.1016/0016-7037(93)90419-w
- 1798 Zharikov AV, Vitovtova VM, Shmonov VM, Grafchikov AA (2003) Permeability of the rocks from  
1799 the Kola superdeep borehole at high temperature and pressure: implication to fluid dynamics in  
1800 the continental crust. Tectonophysics 370:177–191. doi:10.1016/s0040-1951(03)00185-9
- 1801 Zhu W, David C, T-f W (1995) Network modeling of permeability evolution during cementation  
1802 and hot isostatic pressing. J Geophys Res 100:15451–15464
- 1803 Zhu W, Evans B, Bernabe Y (1999) Densification and permeability reduction in hot-pressed  
1804 calcite: a kinetic model. J Geophys Res 104:25501–25511
- 1805 Zoback MD, Townend J (2001) Implications of hydrostatic pore pressures and high crustal  
1806 strength for the deformation of intraplate lithosphere. Tectonophysics 336:19–30

# Author Queries

Chapter No.: 14

---

<b>Query Refs.</b>	<b>Details Required</b>	<b>Author's response</b>
AU1	Please provide email address for J.A.D. Connolly.	
AU2	Please check if the section cross reference is correct.	
AU3	Please cite Balashov and Yardley (1998) in text.	